Computational and Structural Biotechnology Journal 23 (2024) 2516–2533

Contents lists available at ScienceDirect

Computational and Structural Biotechnology Journal

journal homepage: www.elsevier.com/locate/csbj

Research article

Acidic sphingomyelinase interactions with lysosomal membranes and cation amphiphilic drugs: A molecular dynamics investigation

Simone Scrima [a,b,1], Matteo Lambrughi [a,1], Lorenzo Favaro [a], Kenji Maeda [c], Marja Jäättelä [c,d], Elena Papaleo [a,b,*]

[a] Cancer Structural Biology, Center for Autophagy, Recycling and Disease, Danish Cancer Institute, Copenhagen 2100, Denmark
[b] Cancer System Biology, Section for Bioinformatics, Department of Health and Technology, Technical University of Denmark, Lyngby 2800, Denmark
[c] Cell Death and Metabolism, Center for Autophagy, Recycling and Disease, Danish Cancer Institute, Copenhagen 2100, Denmark
[d] Department of Cellular and Molecular Medicine, Faculty of Health Sciences, University of Copenhagen, Copenhagen 2200, Denmark

ARTICLE INFO

Keywords:
Acid sphingomyelinase
Molecular dynamics simulations
Cation amphiphilic drugs
Ebastine
Loratadine
Lysosomal membrane

ABSTRACT

Lysosomes are pivotal in cellular functions and disease, influencing cancer progression and therapy resistance with Acid Sphingomyelinase (ASM) governing their membrane integrity. Moreover, cation amphiphilic drugs (CADs) are known as ASM inhibitors and have anti-cancer activity, but the structural mechanisms of their interactions with the lysosomal membrane and ASM are poorly explored. Our study, leveraging all-atom explicit solvent molecular dynamics simulations, delves into the interaction of glycosylated ASM with the lysosomal membrane and the effects of CAD representatives, i.e., ebastine, hydroxyebastine and loratadine, on the membrane and ASM. Our results confirm the ASM association to the membrane through the saposin domain, previously only shown with coarse-grained models. Furthermore, we elucidated the role of specific residues and ASM-induced membrane curvature in lipid recruitment and orientation. CADs also interfere with the association of ASM with the membrane at the level of a loop in the catalytic domain engaging in membrane interactions. Our computational approach, applicable to various CADs or membrane compositions, provides insights into ASM and CAD interaction with the membrane, offering a valuable tool for future studies.

1. Introduction

Lysosomes are the cellular organelles known as the recycling centers of the cells and key elements in preserving cellular energy homeostasis [1]. Furthermore, the cellular roles of lysosomes extend beyond degradation and recycling, as they are involved in a broad range of processes, including cell death, metabolic adaptation, and antigen presentation [2,3], and in disease, as in cancer where they are involved in promoting cell growth, invasion, metastasis and drug resistance [4]. In particular, lysosomal membrane permeabilization and leakage (i.e., the release of lysosomal contents into the cytosol) can trigger cell death pathways (i.e., lysosome-dependent cell death) [5,6]. Nevertheless, it has been shown that the lysosomal membrane integrity is dynamically regulated in a widespread range of critical physiological cellular processes [3,7,8] The stability of the lysosomal membrane is ensured by a protective glycocalyx and controlled by numerous lysosomal enzymes, including acid sphingomyelinase (ASM). ASM is a lysosomal and peripheral membrane phosphodiesterase that catalyzes the hydrolysis of sphingomyelins to ceramide and phosphocholine [9,10].

The structure of ASM includes different domains, i.e., a saposin-like domain (residues 86–169), a proline-rich linker (residues 170–197) that connects the saposin domain to the catalytic domain (residues 198–540) (Fig. 1A). Moreover, there is a helical domain at the C-terminus (residues 541–613). The mature form of the protein includes six N-linked glycosylation sites [11–13], and the protein is primarily active as a monomer [12]. ASM coordinates two zinc ions with a trigonal bipyramidal coordination geometry, including two aspartic acids (D208, D280), four histidines (H210, H427, H459, H461), one asparagine (N320), and a catalytic water molecule [11] (Fig. 1A). Moreover, three residues (i.e., N327, E390, and Y490) have been suggested to be involved in substrate binding [11]. The active site geometry could favor proton donation to the oxyanion of the ceramide leaving group by H321 or by H284 [11]. The active site of ASM presents a concave and "bowl-like shape" surface, including the inner surface of the saposin

* Correspondence to: Cancer Structural Biology, Danish Cancer Institute, Copenhagen 2100, Denmark.
E-mail addresses: elpap@dtu.dk, elenap@cancer.dk (E. Papaleo).
[1] These two authors equally contributed to the work

https://doi.org/10.1016/j.csbj.2024.05.049
Received 12 January 2024; Received in revised form 30 May 2024; Accepted 31 May 2024
Available online 2 June 2024

domain, where it recruits and binds sphingomyelin and other lipid substrates. It has been shown that ASM has a broad lipid substrate specificity in vitro and can process several membrane phospholipids, including ceramide-1-phosphate and bis(monoacylglycero)phosphate (BMPs) [9]. Thus, it has been proposed that ASM could play a key role in phospholipid catabolism, acting as a promiscuous phospholipase [9]. ASM is suggested to pH-dependently anchor at the membranes of the intralysosomal luminal vesicles, which are known to be the platform for the catabolism of lipids [12], being tethered by the presence of anionic phospholipids, such as BMPs [14]. The membrane anchor allows ASM activity and when the interaction with the membrane is lost or altered, the protein is rapidly inactivated and degraded by cathepsins [6,14]. Nevertheless, the conformations and dynamics of ASM when associated with the lysosomal membrane, such as in the recruitment of lipids at the catalytic site, are unclear. The work of Xiong et al. [12] provided insight into the association of ASM to a lipid bilayer composed of anionic 1-palmitoyl-2-oleoyl-sn-glycero-3-phosphoglycerol lipids using μs coarse-grain molecular dynamics (MD) simulations. The authors observed two lipid-binding modes involving the saposin domain: a) type I and b) type II [12]. The type I association was characterized by the partial insertion of the saposin domain into the lipid headgroup region of the bilayer, where helices H1, H2, and H4 predominantly make contact with the lipids. In contrast, the type II association presented a more open conformation of the saposin domain, allowing all four

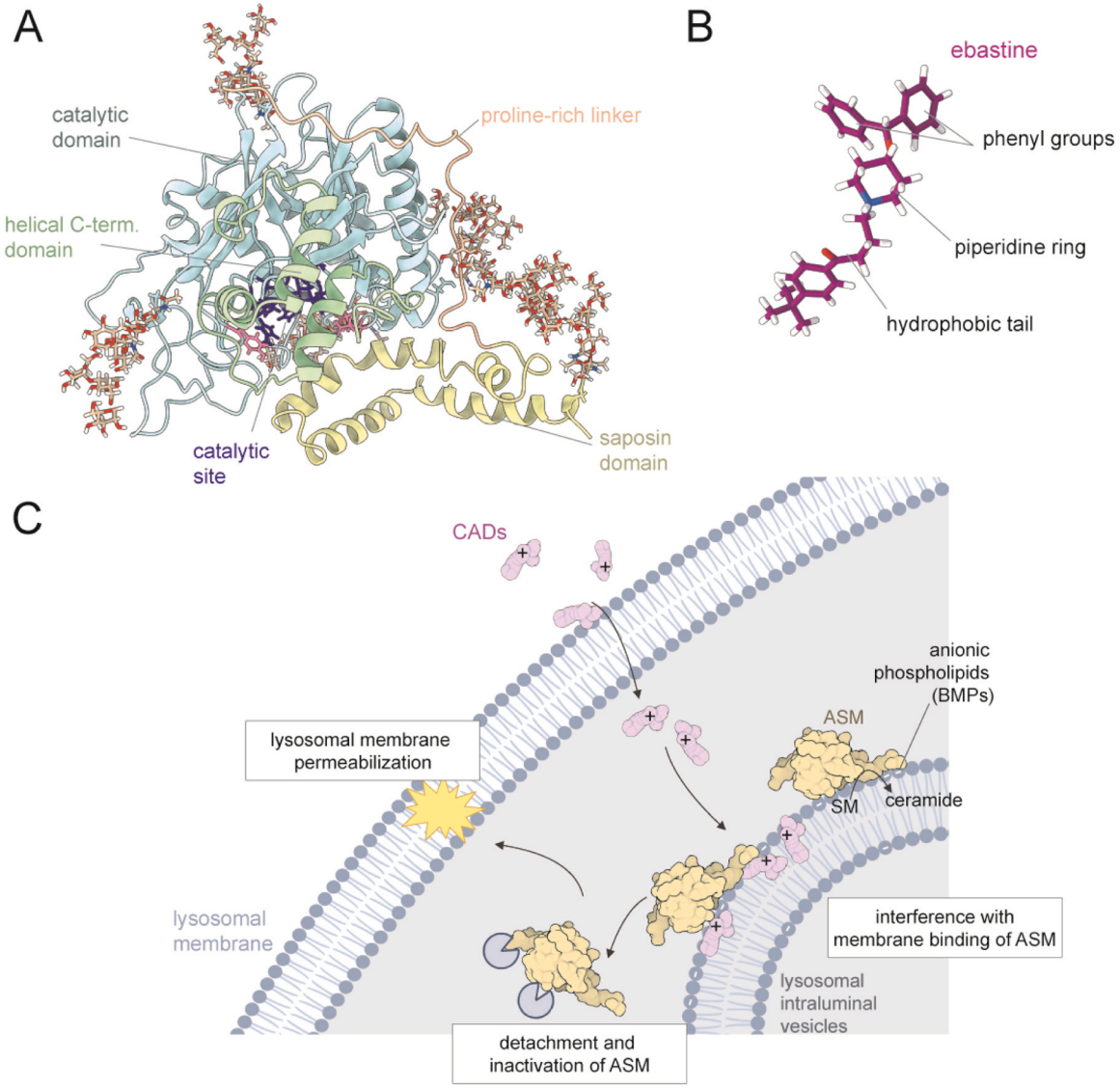

Fig. 1. Mechanisms of ASM and cationic amphiphilic drugs. (A) Structure of human ASM as cartoon representation, highlighting its distinct domains: the saposin domain (residues 86–169, yellow), the proline-rich linker (residues 170–197, light brown), the catalytic domain (residues 198–540, light blue), and the helical domain at the C-terminus (residues 541–613, light green). The catalytic site of ASM, characterized by a concave shape, coordinates two zinc ions (depicted as black spheres). The zinc-coordination residues (D208, D280, H210, H427, H459, H461, N320) and the two residues that may facilitate proton donation in the catalytic mechanism are shown as blue sticks. Additionally, three residues (N327, E390, and Y490), suggested to be important for substrate binding, are represented as pink sticks. The N-glycosylation sites are illustrated as light brown sticks. (B) Structure of ebastine, a cationic amphiphilic drug (CAD). CADs typically possess a hydrophobic group and one or more hydrophilic, basic groups, such as the tertiary amine group in the piperidine ring of ebastine. (C) Proposed anticancer mechanisms of CADs. The mechanism suggests that unprotonated CADs can passively diffuse across lysosomal membranes, becoming protonated and trapped inside the lysosomes. Here the positively charged CADs can insert in the lysosomal intraluminal vesicles and interact with anionic lipids like BMPs, crucial for ASM tethering. This could disrupt the binding of ASM to the membrane, leading to its dissociation and cathepsin-mediated degradation. The resulting accumulation of sphingomyelin and lysoglycerophospholipids may cause lysosomal membrane permeabilization, releasing cathepsins and cytotoxic contents into the cytosol, thus initiating lysosome-dependent cell death. The illustration has been created with BioRender.com.

helices, H1–4, to form contacts with lipids [12].

Notably, ASM and lysosomes are targets of interest that can be potentially exploited in cancer therapy [6,15,16]. Growing data reveal that cancer cells, especially in metastatic cancers, undergo alterations in their lysosomes, including changes in lipid composition, that, while allowing escaping from apoptosis induced by therapy, increase sensitivity to lysosome-dependent cell death [17,18]. Clinically relevant drugs were reported to induce lysosomal permeabilization and lysosome-dependent cell death in cancer cells [19,20]. Several of them are cationic amphiphilic drugs (CADs), which have multiple putative anti-cancer activities, including acting as functional inhibitors of ASM [6,19,21–23]. Several studies reported the potential of CADs against cancer, showing their cancer-specific cytotoxicity against a wide range of cancer cells. Their effectiveness in animal cancer models and pharmaco-epidemiological studies suggested better outcomes for cancer patients taking CADs [6,24,25]. CADs, such as ebastine and loratadine, are a diverse group of pharmacological compounds used to treat various human conditions, including allergies, mental health disorders, cardiovascular diseases, and infections [6]. CADs generally include a hydrophobic part, often made up of aromatic or aliphatic rings, and one or more hydrophilic and basic groups, such as amine groups (Fig. 1B). The proposed mechanism of anticancer action of CADs suggests that due to their basic and amphiphilic nature, they can diffuse across the lysosomal membrane and then be protonated and trapped inside the lysosomes [26–28] (Fig. 1C). The accumulation of CADs in the lumen of lysosomes increases the lysosomal pH [22] and CADs could embed into the membranes of the intraluminal lysosomal vesicles [28], which are the sites of lysosomal lipid degradation, to which ASM and other lysosomal lipases anchor to interact with their lipid substrates [14] (Fig. 1C). Here, CADs could interact with anionic lipids required for the tethering of ASM to the lysosomal intraluminal vesicles, altering the binding of ASM to the membrane and allowing cathepsin-mediated degradation [19,29] (Fig. 1C). The consequent accumulation of sphingomyelin and lysoglycerophospholipids induces lysosomal membrane permeabilization, resulting in the release of cathepsins and cytotoxic contents into the cytosol and initiating lysosome-dependent cell death [21,30]. However, several steps of this mechanism are still unclear, including how and if CADs insert within the membranes and impact membrane properties and stability and how they affect ASM anchoring to the membrane and its lipid-protein interactions.

In this study, we used MD simulations to characterize the interaction between the fully glycosylated ASM form and the lysosomal membrane and to understand the effects of ebastine, hydroxyebastine (a metabolite of ebastine) and loratadine, as examples of CADs, on the lysosomal membrane and the ASM protein.

2. Materials and methods

2.1. Design of lipid bilayers

We used the CHARMM-GUI Membrane Builder tool [31] to design a lipid bilayer with a composition resembling a recent model of the membrane of mammalian lysosomes [32] (Table 1). We build a symmetric lipid bilayer of 125 and 125 Å in the x and y dimensions, respectively. The lipid bilayer included a total of 306 lipids per leaflet. We designed two systems with different starting orientations of ASM to the lipid bilayer. In the first system, we modeled ASM as already localized on top of the lipid bilayer by using the initial configuration previously published [33]. In the second system, we avoided imposing extensive starting contacts between ASM and the lipids using an approach similar to the one used for other peripheral membrane proteins [34]. Starting from the orientation of ASM in the first system, we used the CHARMM-GUI Membrane Builder tool to translate the protein of 15 Å along the z-axis and rotate it by 15 and −10 degrees on the x and y-axis, respectively. We solvated the systems in a rectangular box of water molecules of 157 Å and 167 Å in the z dimension for the first and second systems, including around 320 and 340 water molecules per lipid, respectively. We used the lipid2MD tool available in LipidDyn (https://github.com/ELELAB/LipidDyn)[35] to analyze the lipidomics datasets of lysosomes and match each measured lipid species with the corresponding parameters available in CHARMM36m force field [36]. We used these two systems, hereinafter referred to as model 1 and model 2 for the former and latter modeling strategy, respectively, as starting structures to perform all-atom MD simulations.

Furthermore, we used the last structure of the trajectory of replicate 1 of model 1 to design the starting structure for MD simulations including ASM and CADs. We started from model 1 in light of the analysis of contacts between the protein residues and the lipids, which pointed out a deeper insertion of the saposin domain into the membrane than what was observed for the simulations starting from model 2. We verified that the last structure of replicate 1 of MD simulations for model 1 represented the entire trajectory through structural clustering with the GROMOS algorithm [37] on the Cα-atoms Root Mean Square Deviation (RMSD) matrix.

2.2. MD simulations

We used the MD simulation of model 1 previously published [33] and performed two additional all-atom MD simulations of one-μs each for ASM embedded in a lipid bilayer with a mammalian "lysosomal-like" composition [32] with the CHARMM36m force field [36]. Moreover, we carried out one additional simulation using model 2 (Table 1).

To study the effects induced by ebastine and other CADs, we also performed additional replicates of 500 ns for the same bilayer, including ebastine (EBAH), as well as ebastine and ASM (EBAH-ASM), hydroxyebastine and ASM (OH_EBAH-ASM) and loratadine and ASM (LORA-

Table 1
Summary of the molecular dynamics simulations included in the study.

System	Starting distance of protein from the bilayer (Z-axis, Å)	Temperature (K)	Headgroup molar ratio	N° lipids	Simulation time (μs)	N° replicates
Model 1 ($ASM_{1\ 86\text{-}613}$)	0	310	PC:PE:PI:PS:SM:CHOL:BMP (35:25:8:3:6:18:7)	612	1	3
Model 2 ($ASM_{2\ 86\text{-}613}$)	15	310	PC:PE:PI:PS:SM:CHOL:BMP (35:25:8:3:6:18:7)	612	1	1
EBAH-ASM Model 1 + ebastine ($ASM_{1\ 86\text{-}613}$)	0	310	PC:PE:PI:PS:SM:CHOL:BMP (35:25:8:3:6:18:7)	612	0.5	3
EBAH bilayer + ebastine	N.A.	310	PC:PE:PI:PS:SM:CHOL:BMP (35:25:8:3:6:18:7)	612	0.5	3
OH_EBAH-ASM Model 1 + hydroxyebastine ($ASM_{1\ 86\text{-}613}$)	0	310	PC:PE:PI:PS:SM:CHOL:BMP (35:25:8:3:6:18:7)	612	0.5	1
LORAH-ASM Model 1 + loratadine ($ASM_{1\ 86\text{-}613}$)	0	310	PC:PE:PI:PS:SM:CHOL:BMP (35:25:8:3:6:18:7)	612	0.5	1

ASM) with the CHARMM36m force field [36]. To this goal, we used the force field parameters for CADs obtained as described in the section below (Table 2 **and** Table S1). For the systems with CADs and ASM attached to the membrane, we used the last frame of replicate 1 of model 1 as a starting structure. We designed the MD simulations with CADs following an approach recently applied to other CAD-like molecules [34]. In this study, the authors performed simulations of lipid bilayers, including a membrane protein, with an overall system size comparable to our systems. They used two different CAD densities, i.e., a CAD/lipid ratio of 4.6 % and 9.2 % (equivalent to 24 and 48 CAD molecules, respectively). We thus included CADs in the systems with and without ASM at a density of 6 % CADs/lipid ratio (equivalent to 37 CAD molecules). We used the *insert-molecules* tool of GROMACS to randomly insert the CAD molecules into the box of water molecules. We used a solvent model TIP3P adjusted for CHARMM force fields with Lennard-Jones sites on the hydrogen atoms. We carried out the simulations at a concentration of 0.15 M of NaCl, neutralizing the net charge of the system.

We minimized and equilibrated the systems following the standard CHARMM-GUI Membrane Builder protocol. The protocol consists of multiple equilibration steps, which gradually release positional and dihedral restraints, described by harmonic restraints, applied to the protein and membrane. In addition, we performed a final equilibration, releasing the restraints mentioned above. Firstly, we performed 10,000 steps of minimization by the steepest descent method. Following, two short simulations in the canonical ensemble (i.e., NVT) of 250 ps with an integration step of one fs, using Berendsen thermostat [38] with a coupling constant of one ps, to reach the desired temperature of 310 K. The two thermalization phases were followed by four pressurization steps constituted by 250 ps, 500 ps, 500 ps, and five ns with an integration step of one, two, two, and two fs, respectively. Regarding all the steps, the pressure was controlled semi-isotropically using Berendsen barostat [38], with a time constant of five ps. The final equilibration to finalize the systems lasted five ns with an integration step of two fs.

The productive simulations were performed using a time step of two fs in the NPT ensemble, employing the Nose-Hoover thermostat [39] and the Parrinello-Rahman barostat [40,41] with a time constant of one ps and five ps, respectively. In addition, the LINCS algorithm [42] was used to constrain heavy-atom bonds and the cutoff for both Van Der Waals and Coulomb interactions was set to 12 Å, as well as the particle-mesh Ewald scheme with a 1.2 Å grid spacing [43,44].

2.3. Parametrization of CHARMM36m force field for CADs using CGenFF

We retrieved the two-dimensional (2D) chemical representation of CADs as SDF format files from the PubChem database (ebastine: PubChem entry https://pubchem.ncbi.nlm.nih.gov/compound/3191, CID:3191; hydroxyebastine: PubChem entry https://pubchem.ncbi.nlm.nih.gov/compound/11992145, CID:11992145; loratadine: PubChem entry https://pubchem.ncbi.nlm.nih.gov/compound/ 3957, CID: 3957) [45]. We then used GYPSUM-DL v.1.1.5 [46] to convert the 2D representation of CADs into 3D models and define the appropriate protonation states at the selected pH. For the calculation with GYPSUM-DL, we used 4.5–5.0 and 7.0–7.5 as pH ranges to be considered, and we used default values for the other parameters. For each pH range, we generated ten conformers for each compound. We then selected two conformers for the next parametrization steps: i) one with the protonation state that should be predominant at pH 4.5–5.0 (i.e., lysosomal pH) [47] and ii) one for the form presents at pH 7.0–7.5 (i.e., cytosol pH) [48]. We parametrized both the protonation states of CADs to check that the generated parameters and topologies were consistent with each other. We used open Babel 3.1.1 [49] to convert the output files from GYPSUM-DL into mol2 format files. We employed the stand-alone version of the CHARMM General Force Field (CGenFF) program v. 2.5.1 (SilcsBio) [50]. CGenFF automatizes the generation of force field parameters by defining molecule topology, atom typing, atomic charge assignment, and parameters based on analogy to existing parametrizations in the target force field. CGenFF provides a penalty score for each atomic charge and parameter assigned, evaluating their analogy to existing parameters (i.e., low penalty scores mean good analogy). We calculated the parameters for CADs using as targets the already available parameters in the all-atom CGenFF 4.6 [51]. We verified that in the set of parameters we developed no terms with penalty scores greater than 50 which would require further optimization, such as by ab initio calculations. The only high penalty score was associated with the parameters of a dihedral angle in the pyridinium ring of loratadine. We then

Table 2
New force-field parameters for ebastine derived using CHARMM General Force Field (CGenFF) by analogy to existing parameters in the all-atom CHARMM36m CGenFF 4.6 force field.

Ebastine EBAH							
Total charge	1						
CGenFF penalty scores							
param. penalty	34.000						
charge penalty	24.190						
Angle parameters							
i	***j***	***k***	**θ0 *(deg)***	**kθ *(kJ mol−1 rad−2)***	***info***		
CG2R61	CG311	OG301	110.1	633.4576	*from CG2R61 CG321 OG302, penalty= 4.5*		
CG311	OG301	CG311	109.7	794.9600	*from CG321 OG301 CG321, penalty= 1.2*		
Dihedral parameters							
i	***j***	***k***	***l***	**φ0 (deg)**	**kφ (kJ mol−1)**	***mult.***	***info***
CG2R61	CG2O5	CG321	CG321	0	1.673600	1	*from CG2R61 CG2O5 CG321 CG331, penalty= 0.9*
CG2R61	CG2O5	CG321	CG321	180	0.711280	2	*from CG2R61 CG2O5 CG321 CG331, penalty= 0.9*
CG2R61	CG2O5	CG321	CG321	180	0.543920	3	*from CG2R61 CG2O5 CG321 CG331, penalty= 0.9*
CG2R61	CG2O5	CG321	CG321	180	0.418400	6	*from CG2R61 CG2O5 CG321 CG331, penalty= 0.9*
CG2R61	CG2R61	CG311	OG301	0	0.000000	2	*from CG2R61 CG2R61 CG321 OG302, penalty= 4.5*
OG301	CG311	CG321	CG324	180	2.092000	1	*from OG311 CG311 CG321 CG324, penalty= 15*
OG301	CG311	CG321	CG324	0	2.928800	2	*from OG311 CG311 CG321 CG324, penalty= 15*
OG301	CG311	CG321	CG324	0	1.673600	3	*from OG311 CG311 CG321 CG324, penalty= 15*
OG301	CG311	CG321	CG324	0	1.673600	5	*from OG311 CG311 CG321 CG324, penalty= 15*
CG2R61	CG311	OG301	CG311	180	0.418400	1	*from CG2O2 CG321 OG301 CG331, penalty= 34*
CG2R61	CG311	OG301	CG311	0	3.347200	2	*from CG2O2 CG321 OG301 CG331, penalty= 34*
CG2R61	CG311	OG301	CG311	0	3.347200	3	*from CG2O2 CG321 OG301 CG331, penalty= 34*
CG321	CG311	OG301	CG311	0	2.468560	1	*from CG311 CG311 OG301 CG331, penalty= 2.1*
CG321	CG311	OG301	CG311	0	1.673600	3	*from CG311 CG311 OG301 CG331, penalty= 2.1*
HGA1	CG311	OG301	CG311	0	2.050160	3	*from HGA1 CG311 OG301 CG331, penalty= 1.5*
CG2O5	CG321	CG321	CG324	0	1.188256	3	*from CG2O5 CG321 CG321 CG314, penalty= 0.6*

converted the novel parameters from the format compatible with CHARMM software to the one of GROMACS (see Python script in OSF repository). Finally, we included the topologies and the parameters for CADs in the version for GROMACS 2022 of CHARMM36m [36] and CGenFF 4.6 [51]. All the produced topologies and parameters for ebastine, hydroxyebastine and loratadine and a version of the CHARMM36m/CGenFF force field are available in the OSF repository associated with the publication.

2.4. Analysis of MD simulations

We calculated the main chain RMSD over the MD simulations using as a reference the starting X-ray crystallographic structure of ASM (PDB ID 5I85). We used the main chain atoms of the secondary structural elements of the catalytic domain of ASM for superposition and calculated RMSD of the main chain atoms of i) all the protein, ii) catalytic domain, iii) saposin domain, iv) β1-α1 loop and v) C-terminal domain. We used LipidDyn [35] to calculate i) thickness, ii) area per lipid (APL), and iii) a two-dimensional lipid density map. In addition, we employed a new module of LipidDyn developed to calculate the mean (*H*) curvature of the bilayer. The implementation of the bilayer curvature module was officially included in the LipidDyn GitHub repository on 17/01/2023 (https://github.com/ELELAB/LipidDyn/pull/121). LipidDyn uses the *LeafletFinder* class of MDAnalysis [52] to identify the leaflets of the bilayer and the lipids belonging to them, considering their headgroup for representative atoms of each lipid molecule. LipidDyn estimates the bilayer thickness as the distance vector between neighborhood-averaged coordinates of each lipid and its neighbors in the opposite leaflet, using a cut-off distance of 60 Å. Furthermore, APL is calculated by a neighbor search of each lipid and computation of a Voronoi tessellation. LipidDyn provides not only lipid density maps, using a density calculation algorithm analogous to the *densmap* tool of GROMACS, but also an estimate of the average lipid density during the simulation time [53]. LipidDyn also employs a reimplemented version of the *MembraneCurvature* tool, available in MDAnalysis [https://github.com/MDAnalysis/membrane-curvature/], to derive the membrane surface using lipid headgroups as reference atoms and then estimate mean curvature. For the comparison between the systems including CADs and ASM (EBAH-ASM, OH_EBAH-ASM and LORA-ASM) and model 1, the membrane biophysical properties were computed also over the last 200 ns of the replicates.

We used a protocol previously applied to other cases to investigate the association of ASM with the bilayer and estimate the contacts between protein residues and lipids [54]. In particular, we calculated the number of lipid atoms contained within a spherical surround with a radius of 6 Å around every protein atom during i) all the trajectory time and ii) over the last 500 ns of the trajectory. We also analyzed, in a similar manner, the lipids in contact with the zinc ions or with a selection of residues in the proximity of the catalytic site. In the analysis, we did not consider residues for which each atom featured contacts with the lipids for less than 20 % of the MD frames.

To investigate the interaction mode of the CAD molecules with the lipid bilayer, we employed the *density* tool from GROMACS to calculate mass density profiles along the z-axis of the simulation box. These profiles were generated for all atoms of CADs and the lipids and specifically for the heavy atoms of chemical groups of each CAD, such as the piperidine group, hydrophobic tail, and phenyl group of ebastine. Additionally, we calculated the profiles for the heavy atoms of the lipid headgroups and their backbone and tails. This analysis was carried out on the final 200 ns of each simulation replicate. We chose this timeframe to ensure that nearly all the ebastine molecules had consistently integrated into the bilayer in the EBAH systems. Furthermore, we calculated the contacts between the ebastine and the membrane, i.e., we calculated the number of lipid atoms of each species in the vicinity of each ebastine molecule. Specifically, we used the GROMACS tools to calculate the number of lipid atoms of each lipid species in the vicinity of all the heavy atoms of the piperidine group of ebastine, using a distance cutoff of 6 Å. We then calculated the depletion-enrichment factor [55] around the piperidine group of ebastine of each lipid species as the depletion-enrichment factor of lipid species *X*:

$$D-E = \frac{\left(\frac{\text{(num atoms lipid species X)}}{\text{(num atoms all lipid species)}}\right)_{\text{around 0.6 of piperidine group of ebastine}}}{\left(\frac{\text{(num atoms lipid species X)}}{\text{(num atoms all lipid species)}}\right)_{\text{in bulk membrane}}}$$

Depletion-enrichment factor values above 1 indicate enrichment of the lipid species, while values below 1 indicate depletion. We conducted a bootstrap analysis to determine the 95 % confidence intervals for the median of the depletion-enrichment factor values of each lipid species, setting the number of resamples to 1000 (see OSF repository). Similar to the density analysis mentioned earlier, this analysis was performed on the last 200 ns of each replicate of EBAH.

We calculated pairwise atomic contacts among the heavy atoms of CADs and the ones of the protein using CONtact ANalysis (CONAN) [56] to analyze interactions between ASM and CAD molecules in the MD replicates. We applied a r_{cut} cutoff of 10 Å, $r_{inter,}$ and $r_{high\text{-}inter}$ values of 4.5 Å. Residues with less than 20 % contact with CADs in the simulation frames were excluded from further analysis due to their low occurrence. We then combined this data with information on pocket residues of ASM as reported in [33] to evaluate if CADs could contact sites for ASM association with the lysosomal membrane.

3. Results and discussion

3.1. Analysis of lipidomics data of lysosomes of HeLa and U2OS cells

To study the binding of ASM to the membrane, we designed bilayers as models of lysosomal membranes by analyzing lipidomic datasets of lysosomes of HeLa and U2OS cells [57,58]. The lysosomes were previously isolated by immunoaffinity purification using an antibody against the lysosomal-associated membrane protein 1 and profiled by performing quantitative mass spectrometry-based shotgun lipidomics analysis [57–60]. More than 300 lipid species of 28 different lipid classes of the categories of glycerolipids, fatty acyls, glycerophospholipids, sphingolipids, and sterol lipids were quantified as molar percentages (mol%, molar quantity normalized relative to the total molar quantities of all the identified lipids) [57,58] (Fig. 2A). We compared these lipidomics data with the lipid compositions of a recent computational model of the membrane of mammalian lysosomes (Fig. 2A) [32]. The two cell lines show very similar lipid compositions for their lysosomes (Fig. 2A). Cholesterol, phosphatidylcholine and phosphatidylethanolamines are the most abundant lipids in all three datasets. The main difference is associated with the higher percentage of cholesterol in both U2OS and HeLa cells, while phosphatidylethanolamines are overrepresented in the computational model (Fig. 2A). On the other hand, the content of lysosome-specific BMP (phosphatidylglycerol-BMP) and sphingomyelin classes are consistent across the three datasets, accounting for around 2.3–2.8 mol% and 8–6 mol% of lipids in the lipidomics datasets and around 7 % and 6 % in the computational model, respectively (Fig. 2A). When considering the lipidomic data, it is essential to note that the samples encompass both the external lysosomal membranes and the intralysosomal luminal vesicles. BMPs localize primarily at the intralysosomal luminal vesicles where ASM anchors and plays its activity [61]. Consequently, one would expect that the BMP mol % should be higher in lipidomics of purified intralysosomal luminal vesicles. Given the overall similar patterns of lipid compositions between the lipidomic dataset of lysosomes of HeLa and U2OS cells and the computational model, we designed our lipid bilayer to resemble the latter.

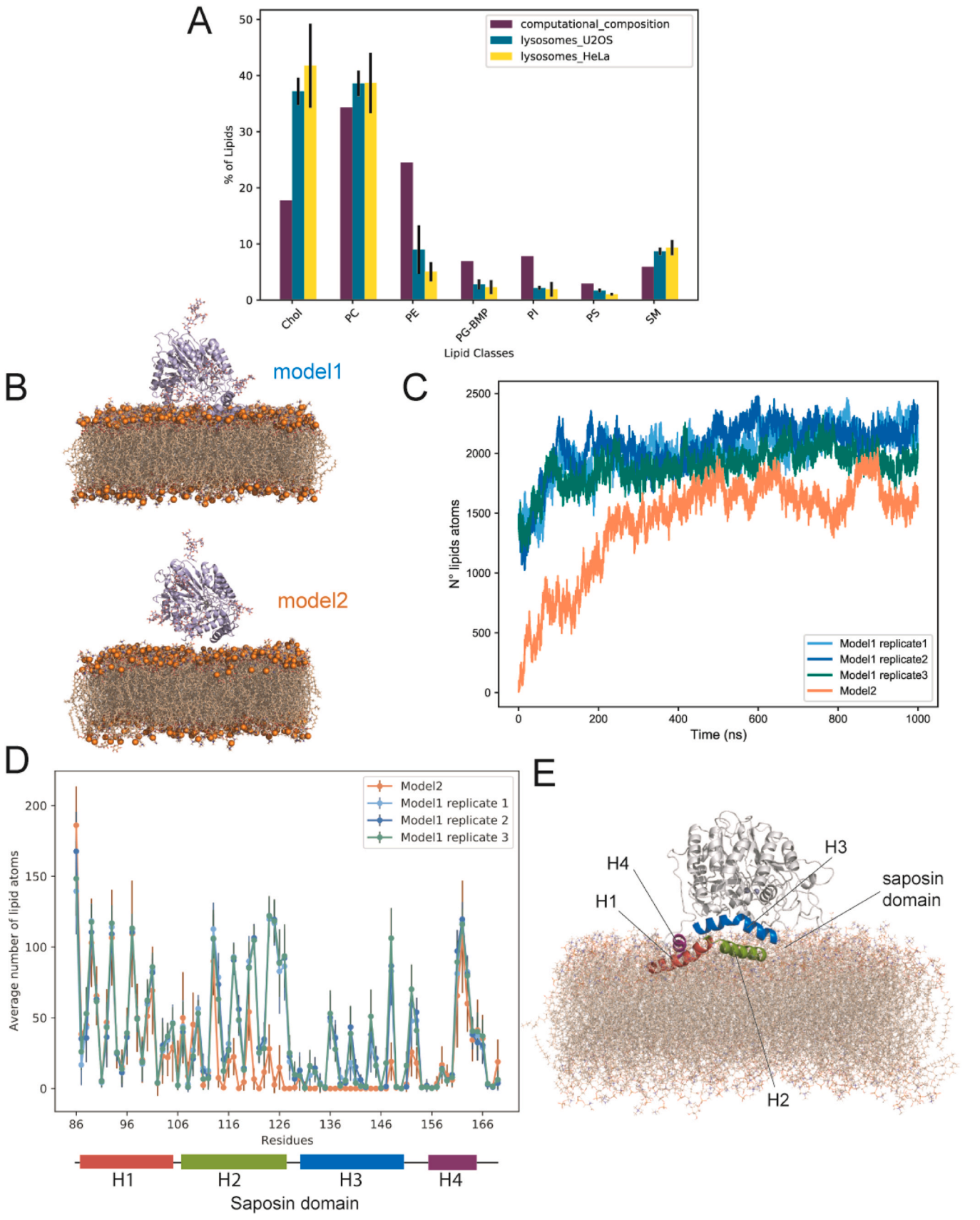

(caption on next page)

Fig. 2. ASM interacts with lipid bilayers resembling lipid compositions of lysosomal membranes in all-atom MD simulations. (A) Mass spectrometry-based shotgun lipidomics profiles of immunopurified lysosomes from HeLa (yellow bars) and U2OS (green bars) cells, compared with a computational model of mammalian lysosomal membranes (purple bars). The two cell lines show very similar lipid compositions. The analysis reveals similar lipid compositions across the two cell lines and the model, consistent with lysosome-specific BMPs-phosphatidylglycerol (PG) and sphingomyelin (SM) classes. (B) Two modeling strategies were used to start the MD simulations: i) model 1, where ASM is positioned directly in contact with the bilayer surface (upper panel), and model 2, where ASM is initially distanced from the bilayer (lower panel). ASM is represented as a blue cartoon, and the lipids are shown as light brown sticks with phosphate groups in their headgroups highlighted as orange spheres. (C) The number of lipid atoms in contact with ASM during the MD simulations shows the spontaneous association of ASM in both model 1 and model 2. (D) The average number of lipid atoms in contact with the saposin domain of ASM indicates a partial insertion of this domain into the bilayer. Helices H1, H2, and H4 are predominantly involved in the interaction with the bilayer. (E) An example of the orientation of ASM when in contact with its saposin domain to the lipids was observed from replicate 1 of model 1.

3.2. Interaction between ASM and the lysosomal membrane

To characterize the interaction between ASM and the lysosomal membrane, we collected four one-μs all-atom MD simulations of the protein with the lipid bilayer (Table 1), employing two strategies to predict how they associate (Fig. 2B). A model and its first MD simulation (i.e., replicate 1 of model 1) are taken from our recent study [33]. This initial system for MD simulations had ASM positioned on the bilayer surface and interacting with the lipids. We performed two additional MD replicates for this configuration (Table 1). Secondly, we carried out one additional MD simulation, positioning the protein 15 Å away from the bilayer, along the axis perpendicular to the surface of the bilayer. This was done to avoid extensive contact, following a previously suggested approach [34]. We will refer hereinafter to model 1 and model 2 (Fig. 2B) for the two different initial configurations, respectively. In addition, we accounted for the *N*-glycosylations of ASM in the interaction with the membrane. Hence, we modeled a full oligomannose (Man5) glycosylated variant of ASM (i.e., at the sites N88, N177, N337, N397, N505, and N522), as previously described [33]. We observed that the catalytic domain of ASM largely maintains its X-ray crystallography structure in all the MD replicates of ASM with the lipid bilayer, experiencing only minor fluctuations (Fig. S1). Conversely, the β1-α1 loop of the catalytic domain and the saposin domain exhibit significant flexibility, adopting conformations distinct from those in the starting structure (Fig. S1). The β1-α1 loop extends from the catalytic domain of ASM on the membrane-bound side and localizes near the saposin domain, potentially contributing to membrane binding. We observed that the β1-α1 loop binds lipids and transitions to more open conformations, especially in replicate 1 and 2 of model 1 and in model 2 (Fig. S1). The saposin domain remains integrated within the membrane, forming contacts with lipids.

We investigated the structural properties of the lipid bilayer and the effects induced by the association with ASM. We noticed that the four simulations have a comparable average lipid density of the bilayer (~ 13,000 $Å^{-3}$) (Fig. S2 and OSF repository). However, we observed that in the MD simulation starting from model 1 (i.e., already localized on top of the membrane at the beginning of the simulations), there is a higher density of lipids in several areas of the bilayer, suggesting that they are more ordered and packed (Fig. S2). Furthermore, we calculated the average area-per-lipid and lipid bilayer thickness in the four MD simulations. We observed that MD simulations of model 1 and model 2 have similar values for both area-per-lipid (average 54.0 $Å^2$ and 53.5 $Å^2$, respectively) and thickness (average 40.8 Å and 41.2 Å, respectively) (Fig. S2).

To investigate the association of the protein to the bilayer, we monitored the number of lipid atoms in contact with ASM during the simulation time (Fig. 2**C**). We observed the spontaneous association of ASM in model 2 to the bilayer after 70 ns of simulation time. For model 1, we observed a similar overall trend for the three replicates, and the number of lipids in contact with ASM does not show marked fluctuations after 200 ns of simulation time. It has been suggested that the saposin domain of ASM plays a crucial role in the binding to the membrane [11, 12]. We thus monitored the residues within the saposin domain (residues W86-H169) that are in contact with the lipids in the simulations and compared our results to those obtained from a previous study [12]. Our MD simulations present partial insertion of the saposin domain in the bilayer, mostly involving helices H1, H2, and H4 (Fig. 2D-E). Furthermore, when comparing the lipid contact profiles of model 2 with the three replicates of model 1, we observed that in model 2, there are fewer lipid atoms in contact with helix H2 and H3, indicating a less deep insertion of ASM into the lipid bilayer than observed in model 1 (Fig. 2D). In light of these observations, we focused on the MD simulations from model 1 and its replicates for further analyses. The three replicates of model 1 all have consistent lipid contact profiles, showing a similar interaction with the bilayer. The partial insertion of the saposin domain of ASM into the lipid bilayer resembles a saposin-lipid binding mode previously described (i.e., named type I) (Fig. 2E) [12].

The membrane interactions of ASM are particularly relevant when considering its proposed catalytic mechanism. The active site of the protein is not adjacent to the membrane, but rather distant from its surface (around 20 Å at the beginning of the simulation in model 1). Therefore, ASM, after binding the membrane, needs to recruit the lipids at its active site, where they undergo hydrolysis [11]. We thus investigated if lipids could form atomic contacts with the zinc ions, the catalytic (i.e., H321) and the zinc-coordinating residues (i.e., D208, H210, D280, N320, H427, H459, and H461), along with the suggested substrate-binding residues (i.e., N327, E390, and Y490) (Fig. 3 and S3). We observed that starting from no lipids in their surrounding, all three replicates of model 1 consistently show the substrate-binding residues N327, E390, and Y490 to form contacts with lipids, especially N327 and E390 (occurrence of lipid contact in the range 67.9–93.9 % and 81.5–96.6 % of MD simulation time) (Fig. 3A and S3). N327, E390, and Y490 are located in the catalytic domain of ASM, in particular in the β3-α3, β5-α5 and β9-β10 loop, respectively, at the inner and hydrophobic concave surface of the protein, which faces the membrane (Fig. 3B). In light of our results, N327, E390, and Y490 could play a role in the recruitment and orientation of the substrate lipids towards the catalytic site. We also observed lipid atoms in contact with the residues in the active site, especially involving H321, H459, and H461 in replicate 1 and 2 (occurrence in the range 31.4–91.5 %, 54.6–82.1 %, and 28.2–68.8 % of MD simulation time, Fig. 3A and S3). In terms of lipid species in contact with residues in the surroundings of the active sites, we observed different species, including sphingolipids (e.g., sphingomyelin) and glycerophospholipids (such as phosphatidylcholine, phosphatidylethanolamine, phosphatidylinositol, phosphatidylserine, and BMPs) (Fig. 3C and S3). Our findings align with data from experimental micellar assay systems, which showed that recombinant ASM efficiently hydrolyzes sphingomyelins but also has hydrolytic capabilities, albeit with low efficiency, on a range of other membrane lipid species, including glycerophospholipids, lyso-glycerophospholipids, ceramide-1-phosphate, and BMPs [9]. We noticed that BMPs, which are anionic lipids, form high-occurrence contacts with the zinc ions in replicates 2 and 3 (Fig. S3), which might be due to an overstabilization of the ionic interaction between the metal ions and the anionic lipids in the MD force field used for this study.

To further investigate the mechanism of lipid recruitment around the saposin domain and at the active site of ASM, we monitored the impact of the protein interaction on the membrane curvature (Fig. 4). We observed that ASM induces a negative mean curvature in both bilayer leaflets in all the replicates of model 1, resulting in a dome-like shape

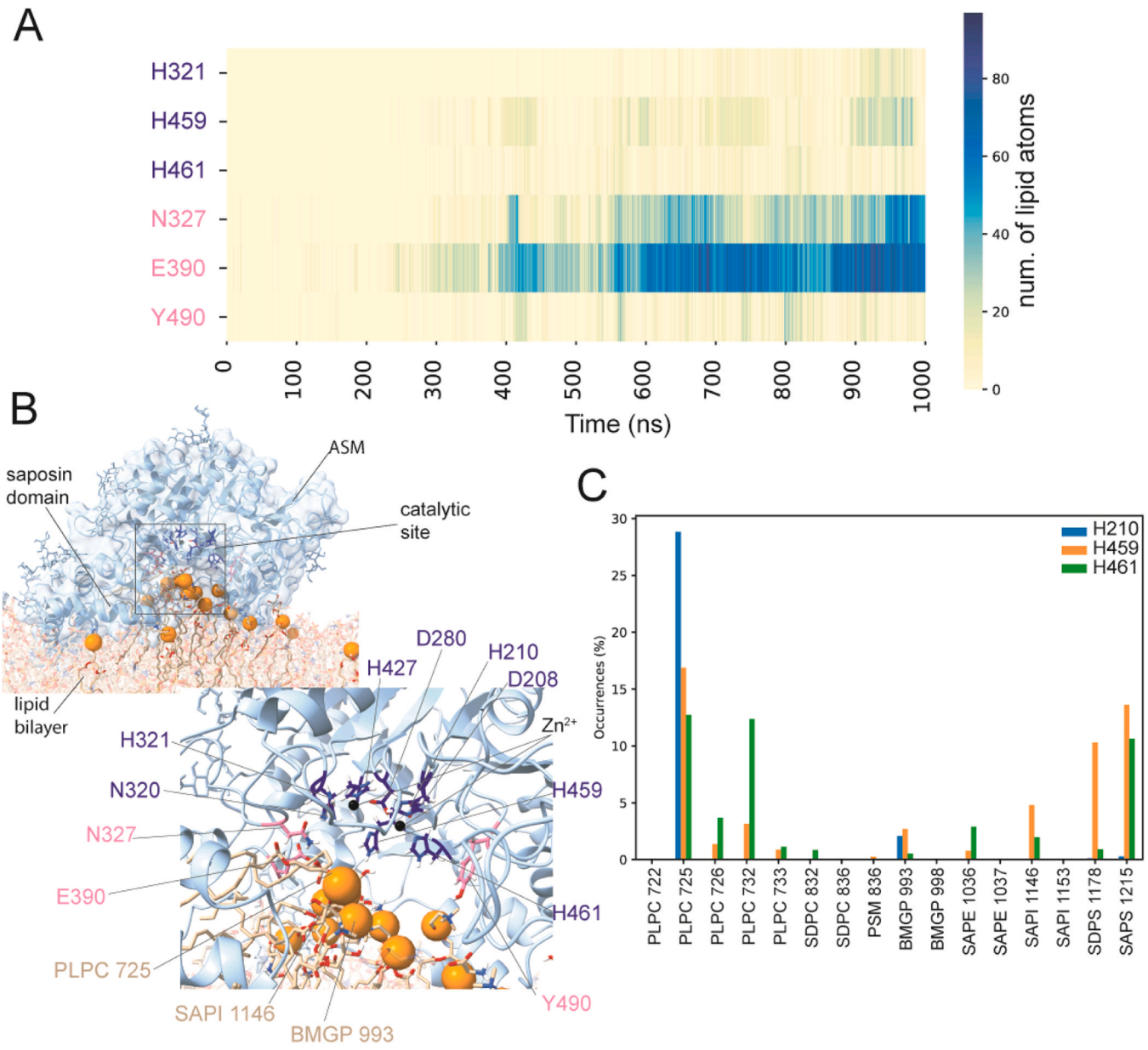

Fig. 3. ASM recruits diverse lipid species at its catalytic site. (A) Heatmap showing the number of lipid atoms in contact with the substrate-binding (N327, E390, Y490), catalytic (H321), and zinc-coordinating residues (H459 and H461) of ASM during the replicate 1 of model 1. The other residues in the active site and the zinc ions featured contacts with the lipids for less than 20 % of the MD replicate. (B) Visualization of the orientation of ASM relative to the lipid bilayer after 900 ns in replicate 1 of model 1. In the upper panel, ASM is shown as a blue cartoon, with lipids contacting the catalytic site residues depicted as light brown sticks, and their phosphate groups are highlighted as orange spheres. The lower panel highlights the orientation of lipids recruited at the active site (light brown) and the substrate-binding (pink), catalytic, and zinc-coordinating (dark blue) residues within the catalytic site of ASM. (C) Diversity of lipid species interacting with the active site residues of ASM during replicate 1 of model 1. The bar plot shows the occurrence of lipid species in forming contact with the residues of ASM. We observed various sphingolipids and glycerophospholipids, suggesting a broad lipid substrate specificity of ASM.

beneath the active site (Fig. 4A-B). The average local mean curvature under the protein active site reaches values as low as $-0.36\ nm^{-1}$ for the upper leaflet in correspondence to the displacement of lipids from the upper leaflet towards the active site of ASM. Furthermore, for replicate 2 of model 1, ASM induces positive curvature in two regions of the bilayer, which correspond to the areas where the saposin domain inserts in the bilayer (Fig. 4B). This observation suggests an effect on membrane curvature due to the insertion of the saposin domain into the bilayer in this replicate. Overall, the curvature induced by ASM to the bilayer in the region next to the saposin and beneath the catalytic site may facilitate the recruitment of lipids to the residues in the catalytic site.

3.3. *Parametrization of Cationic Amphiphilic Drugs: A Case Study with Ebastine*

After investigating the binding of ASM to the lipid bilayer, we focused on studying the effects of CADs on the membrane biophysical properties, lipid-protein interactions, and the ASM structure.

To model CADs in MD simulations, it is necessary to compute the missing force-field parameters to describe the target molecules. Here, we used a workflow based on different computational approaches to define the force-field parameters for ebastine (Fig. 5A) as a representative of cation amphiphilic drugs affecting ASM function at the lysosome (see Materials and Methods). In brief, we calculated the final set of force-field

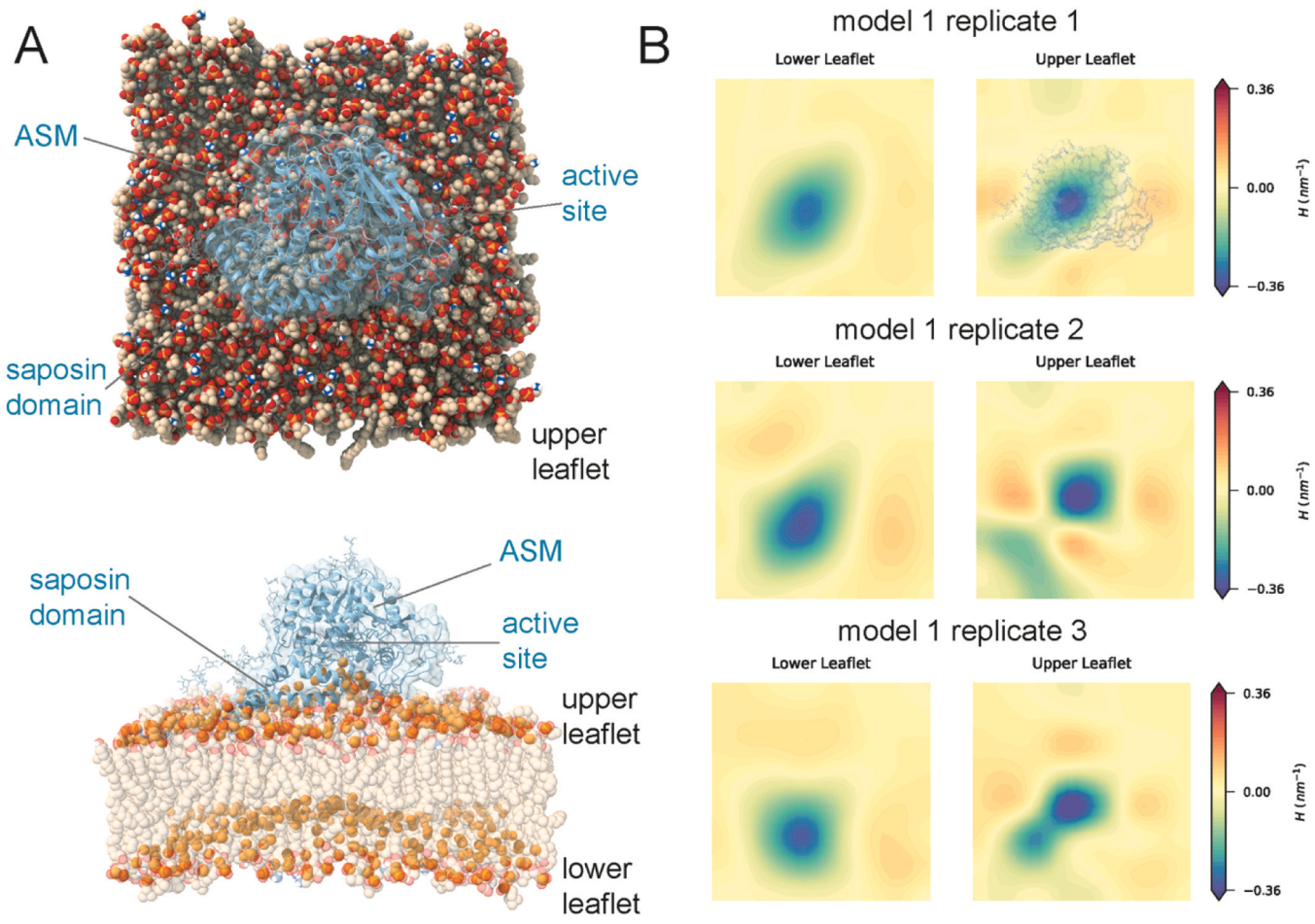

Fig. 4. ASM induces membrane curvature in the bilayers. (A) Structure from replicate 1 of model 1, with an above view (upper panel) and side view (lower panel) of ASM. These views illustrate ASM inducing a negative mean curvature in both bilayer leaflets, resulting in a dome-like formation beneath its active site. (B) Average mean curvature of the lower (left panels) and upper (right panels) leaflets of the bilayer calculated for replicates 1–3 of model 1. Negative and positive mean curvature are indicated in blue and red, respectively. The average local mean curvature under the protein active site reached values as low as −0.36 nm^{-1}. Replicate 2 shows positive curvature in two bilayer regions corresponding to insertion points of the saposin domain, suggesting a deeper insertion of the saposin domain in this replicate relative to the others.

atomic charges and parameters for ebastine by analogy to existing parameters from an established force-field model, frequently used in MD simulations of membranes and small molecules [36,51] (Fig. 5A and Table 2). Ebastine is a basic compound that contains a tertiary amine group, which is protonated at the lysosomal pH of ~4.5–5.0. We thus generated parameters for ebastine for the protonation state that should be predominant at lysosomal pH (Fig. 5B). We found that the force-field atomic charges and parameters we calculated for ebastine matched well with the existing force-field parameters, as shown by their low penalty scores (i.e., lower than 50) (Table 2). This consistency suggested that our parameters are reliable for use in MD simulations of ebastine without needing further refinement. We used our parameters to investigate at the molecular level the interactions and effects of ebastine on membrane and ASM by performing all-atom MD simulations in the presence of ebastine of i) ASM associated with the lysosomal-like bilayer (EBAH-ASM) and ii) the bilayer without the protein (EBAH) (Fig. 5C). We designed the MD simulations with ebastine following an approach recently applied to other CAD-like molecules (see Materials and Methods) [34]. In this study, the authors observed that the amount of CAD molecules used in the simulations (CAD/lipid ratio of 4.6 % and 9.2 %) was enough to induce dose-dependent effects, such as alterations of membrane fluidity, curvature, thickness, and changes in the association of the protein with the membrane [34]. We thus designed our systems with an ebastine/lipid ratio of 6 %.

3.4. How ebastine molecules alter the lysosomal membrane and interact with ASM

At first, we aimed to investigate the effect of ebastine on the lysosomal membrane itself. We thus estimated the number of ebastine atoms in contact with lipids in the MD simulations of the EBAH system (Fig. 6A). We observed the spontaneous insertion of ebastine in the bilayer with more than 80 % of ebastine atoms already in contact with the bilayer after 150 ns and nearly 100 % after 300 ns (Fig. 6A). On the other hand, in the EBAH-ASM system (Fig. 6B), there is an incomplete membrane insertion of ebastine. We observed that after 400 ns of simulation time, ~70–80 % of ebastine atoms are in contact with the bilayer (Fig. 6B). Furthermore, the ebastine molecules integrate into the bilayer from either the upper or the lower leaflets in the EBAH and EBAH-ASM systems (Supplementary videos S1–2).

Supplementary material related to this article can be found online at doi:doi:10.1016/j.csbj.2024.05.049.

To disclose the mode of insertion and integration of ebastine into the membrane, we investigated how ebastine and the main components of lipids are distributed within the thickness of the lipid bilayer. We calculated the mass density profiles of the chemical groups of lipids and ebastine along the axis perpendicular to the surface of the lipid bilayer for each replicate of EBAH and EBAH-ASM (Fig. 6C and Fig. S4). We observed that ebastine is generally inserted in the bilayer at the interface

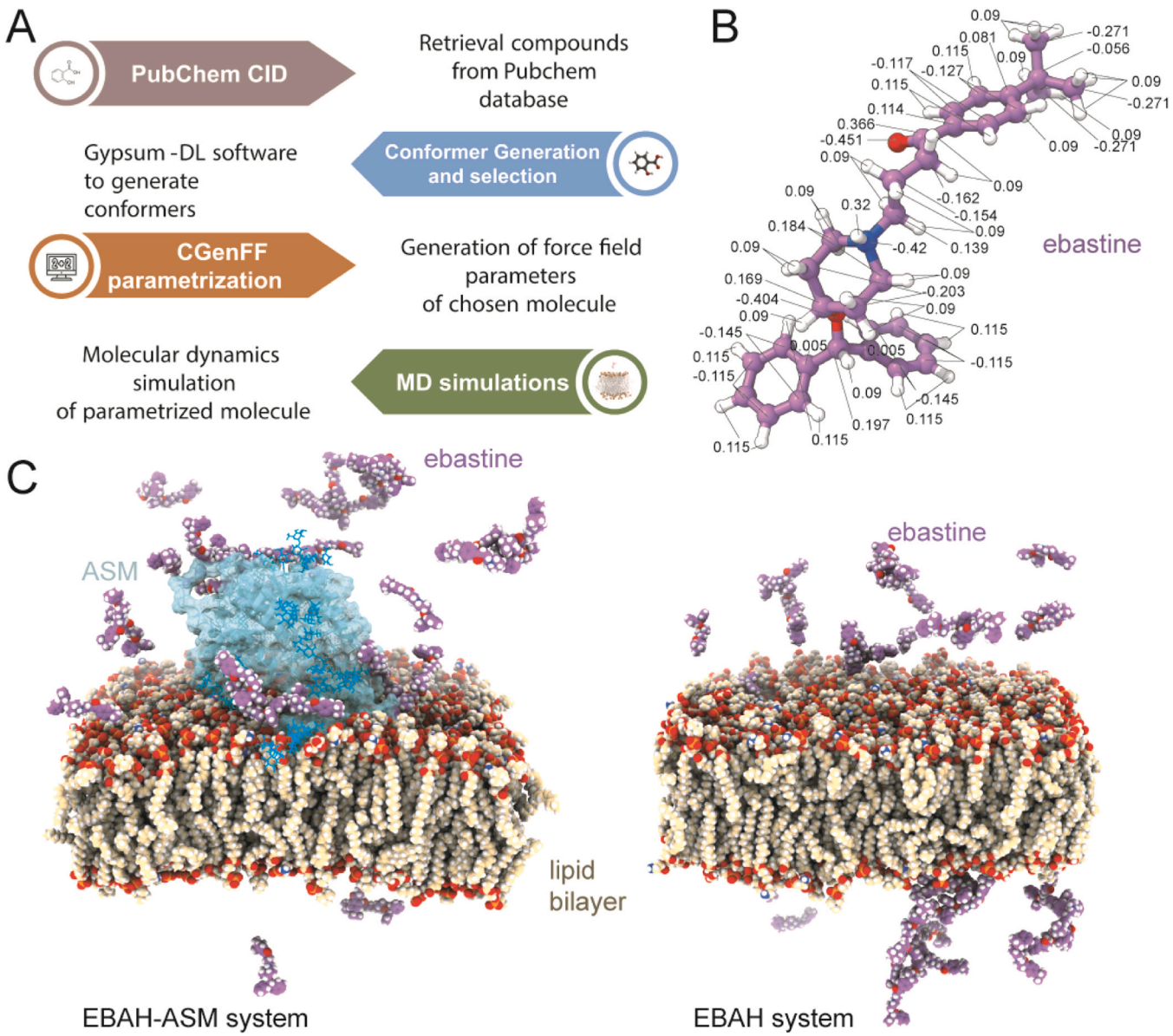

Fig. 5. Force field parametrization of ebastine and design of MD simulations in membrane systems (A) Outlines of the computational workflow used to compute the force-field parameters for ebastine, employing computational approaches such as CHARMM General Force Field (CGenFF) for deriving parameters by analogy to existing parameters in the CHARMM36m/CGenFF4.6 force field. (B) Visualization of the protonation state of ebastine at lysosomal pH, showing the atomic charges obtained by CGenFF. (C) All-atom MD simulation designs of the two systems with ebastine: on the left, the combination of ebastine and ASM associated with the lipid bilayer (EBAH-ASM system); on the right, the lipid bilayer in the absence of the protein (EBAH system). Both systems included an ebastine/lipid ratio of 6 %, a concentration previously shown to induce dose-dependent effects in bilayers with CAD-like molecules.

between lipid headgroups and their backbone-hydrophobic tails (Fig. 6C and Fig. S4). Furthermore, the analysis suggested that ebastine molecules preferentially orient with their hydrophobic tails and phenyl groups towards the lipid tails, while the piperidine rings, featuring the positively charged tertiary amine group, are oriented more towards the lipid headgroups (Fig. 6C and Fig. S4). In the EBAH-ASM systems, we noted a comparable pattern for ebastine (Fig. S4). However, in these systems, the incomplete integration of ebastine into the bilayer results in less-defined density profiles.

We then estimated if the piperidine ring of ebastine, when inserted into the membrane, formed preferential interaction with any of the lipid species used in the modeling. In particular, we estimated the changes in the concentration of each lipid species around the piperidine ring, compared to their concentration in other regions of the membrane, by calculating their depletion-enrichment factor [55] (Fig. 6D and Fig. S5). Depletion-enrichment factor values above 1 indicate enrichment of the lipid species around ebastine, while values below 1 indicate depletion. Our analysis suggested a propensity for the enrichment of anionic lipids in the vicinity of the piperidine ring of ebastine, including phosphatidylinositol, phosphatidylserine species, and BMPs (Fig. 6D and Fig. S5). In detail, we observed an enrichment of BMPs (BMGP) and SAPI across all replicates of EBAH. These ebastine-lipid contacts could be driven by interactions between the positively charged ebastine amine group and the lipid anionic headgroups, as previously proposed for other CAD-like molecules [34,62].

In the presence of ebastine and the absence of the protein, the lipid bilayer has an average lipid density of ~ 14,100 $Å^3$ (Fig. S6), thus slightly increased when compared to the MD simulations with ASM (~ 13,800 $Å^{-3}$). We then calculated the average area per lipid and lipid bilayer thickness in the three replicates of the EBAH system (Fig. 7A and

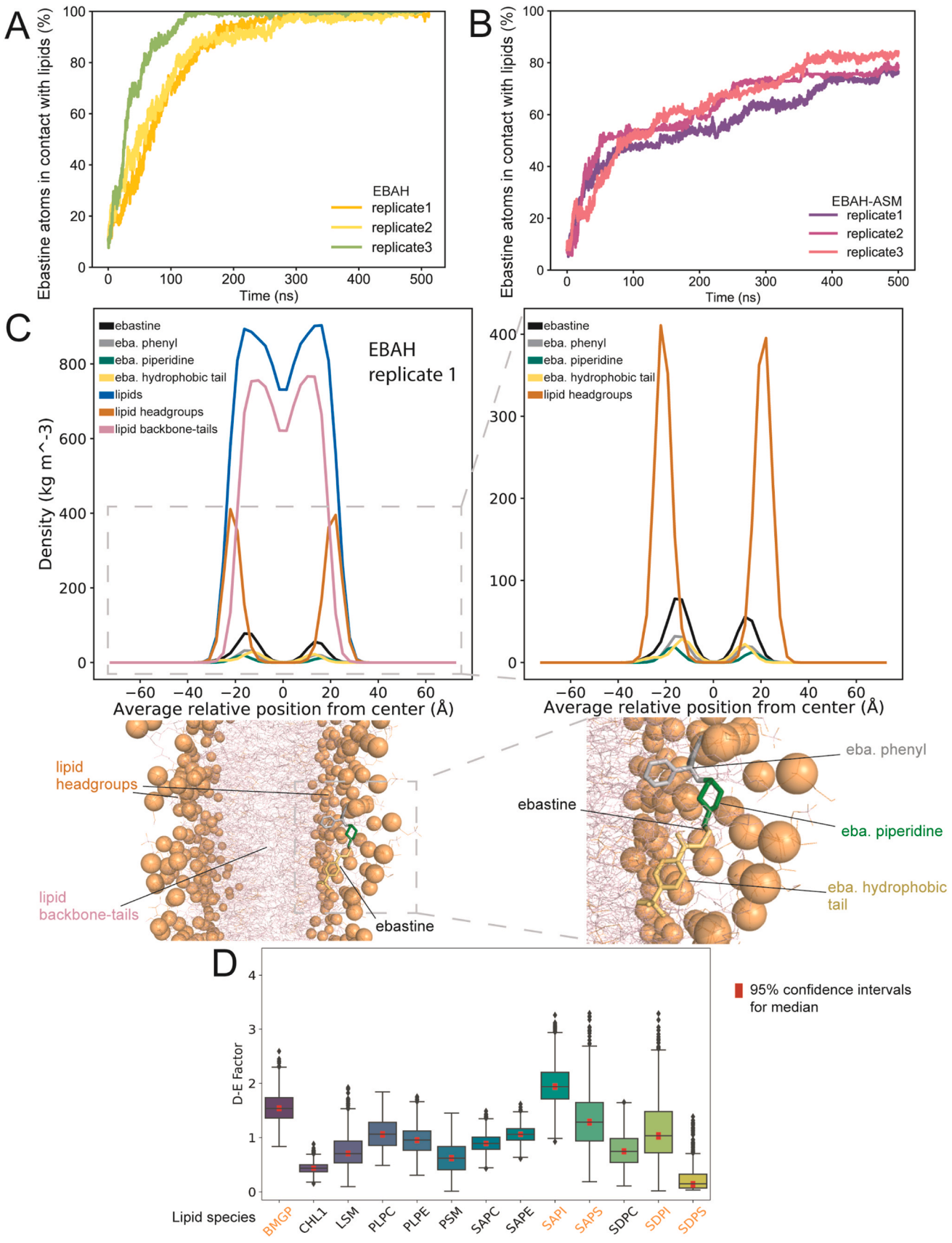

(caption on next page)

Fig. 6. Ebastine interacts with a lysosome-like bilayer and inserts at the interface between lipid headgroups and tails. (A) Percentage of ebastine atoms in contact with the lipid bilayer over time in the EBAH replicates. We observed spontaneous insertion with over 80 % of ebastine atoms in contact with lipids after 150 ns and full insertion after 300 ns. (B) Percentage of ebastine atoms in contact with the lipid bilayer over time in the EBAH-ASM replicates. We observed incomplete insertion of ebastine molecules in the bilayer in the presence of ASM with around 70–80 % of ebastine atoms in contact with lipids after 400 ns. (C) The mass density plots show how ebastine and the main components of lipids are distributed within the thickness of the lipid bilayer. The left upper panel shows the mass density profiles of i) all ebastine atoms (black), ii) ebastine phenyl groups (grey), iii) ebastine piperidine groups (green), iv) ebastine hydrophobic tails (yellow), v) all lipid atoms (blue), vi) lipid headgroups (orange) and v) lipid backbone-tails (pink) along the axis perpendicular to the surface of the bilayer. For clarity, we show the results for replicate 1 of the EBAH system. The results for the other replicates are reported in Fig. S4. The right upper panel highlights the mass density profiles of lipid headgroups and ebastine mass density profiles. The left lower panel shows a bilayer section with an ebastine molecule inserted in the membrane from replicate 1 of the EBAH system for illustrative purposes. Ebastine and lipids are shown as sticks, with the phosphate groups of the lipids highlighted as spheres. The right lower panel highlights the orientation of ebastine in the bilayer. The ebastine molecules insert at the interface between lipid headgroups and hydrophobic tails, with their hydrophobic tails and phenyl groups preferentially orienting towards the lipid tails and the piperidine ring towards the lipid headgroups. (D) The box plot displays the depletion-enrichment factor (D-E factor) for each lipid species in proximity to the piperidine group of ebastine, calculated for replicate 1 of the EBAH system. Depletion-enrichment factor values above 1 suggest enrichment of the lipid species, whereas values below 1 indicate depletion. Anionic lipids are highlighted in orange. The red bars represent the 95 % confidence intervals for the median of the depletion-enrichment factor values of each lipid species, calculated using bootstrapping analysis.

Fig. S6). We observed that the insertion of ebastine in the bilayer slightly increases its area per lipid (average 59.8 ± 0.13 Å^2) and reduces the thickness (average 40.4 ± 0.4 Å) when compared to the reference MD simulations of a bilayer with the same lipid composition but in the absence of ebastine (average APL 56.6 Å^2 and thickness 42.2 ± 0.2 Å) [32]. The thickness profiles over time for EBAH, EBAH-ASM and ASM in the absence of ebastine (model 1) simulations are similar (Fig. S6 and S7), with only a few conformations of EBAH-ASM at lower values of thickness (< 39 Å). The area per lipid profile over time has a similar overall trend in the two systems but reaches a plateau at lower values for EBAH-ASM (average area per lipid 56.6 ± 0.02 Å^2) than EBAH (Fig. S6). The addition of ebastine slightly increases the area per lipid of the bilayer compared to when only the protein was present (Fig. S7). In the absence of the protein, ebastine alone does not induce changes in bilayer curvature (Fig. 7B and Fig. S8). Moreover, ebastine does not have effects on the curvature induced by ASM itself on the bilayer in the EBAH-ASM systems compared to what was observed with the ASM model 1 replicates (Fig. S9).

We evaluated the binding modes of ebastine into the ASM structure using a contact-based analysis combined with the analysis of solvent-exposed pockets of ASM (Fig. 7C-D and Fig. 8) taken from our previous study [33]. According to the previous analysis, pockets 1, 3, 6, 7, 15, and 22 match with regions for ASM-membrane interactions, whereas pockets 5 and 12 include residues near the catalytic site. We observed that ebastine establishes contact with the protein in all the MD replicates within the initial 100 ns (Fig. 7C-D, Supplementary video 3). Furthermore, the interaction with ebastine does not affect the conformation of the catalytic domain, which retains the X-ray crystallography structure in all replicates (Fig. S1). We estimated the occurrence and persistency (Fig. 8A-B and Fig. S10) of the interactions of the ebastine molecules with ASM in the three EBAH-ASM replicates, focusing on contacts formed at least in 20 % of the simulation frames. We observed that ebastine tends to bind to many different regions of the protein but with low occurrence and several events of formation/breaking of the interactions. In addition, we observed the tendency of forming interactions with some of the interfaces for membrane association and no interaction in the proximity of the active site. Furthermore, ebastine molecules interact with residues in the β1-α1 loop (Fig. 8A-B). This loop extends from the catalytic domain and localizes close to the H2, H3 and H2-H3 loop of the saposin domain [11], potentially contributing to membrane binding. Interestingly, we identified that the interaction with ebastine molecules tends to reduce the lipid contacts of the residues in the β1-α1 loop (Fig. 8C).

Supplementary material related to this article can be found online at doi:10.1016/j.csbj.2024.05.049.

Our results suggest that ebastine in high concentration can interfere with the association of ASM with the lysosomal membrane, binding regions of the catalytic domain involved in its anchoring to the bilayer.

3.5. How other CAD representatives alter the lysosomal membrane and interact with ASM: hydroxyebastine and loratadine

After investigating the effects of ebastine, we extended our framework to study the effects of other two CAD representatives: i) hydroxyebastine, a metabolite of ebastine (OH_EBAH) and ii) loratadine (LORAH). We used the same approaches described in Section 3.3 to calculate the set of force-field atomic charges and parameters for these two CAD compounds. We then used these parameters to investigate at the molecular level their interactions and effects on membrane and ASM, by performing all-atom MD simulations in the presence of ASM associated with the lysosomal-like bilayer (OH_EBAH-ASM and LORAH-ASM systems) (Fig. 9).

We observed that both hydroxyebastine and loratadine incompletely insert in the bilayer (Fig. 9A). While hydroxyebastine shows a membrane insertion similar to ebastine, with after 400 ns of simulation time ~70–80 % of hydroxyebastine atoms are in contact with the bilayer (Fig. 9A), loratadine shows a highly incomplete insertion, with only ~55 % of loratadine atoms that form contacts with the bilayer (Fig. 9A). The mass density profiles of the lipid bilayer for the OH_EBAH-ASM system showed that hydroxyebastine molecules are inserted in the bilayer at the level of the interface between lipid headgroups and their backbone-hydrophobic tails (Fig. 9B). The hydroxyebastine molecules preferentially orient their phenyl groups towards the lipid tails and the piperidine ring towards the lipid headgroups, similar to ebastine, while their hydrophobic-OH tails are more oriented towards the lipid headgroups than ebastine, due to the presence of the polar hydroxy group that can form interactions with the lipid headgroups (Fig. 9B). The highly incomplete integration of loratadine into the bilayer in the LORAH-ASM system results in less defined mass density profiles suggesting that loratadine molecules localize at the level of lipid headgroups (Fig. S11). We observed that the insertion of hydroxyebastine or loratadine in the bilayer does not largely affect the area per lipid and thickness of the bilayer (Fig. S11). In particular, the insertion of hydroxyebastine shows a similar effect as ebastine with a slight increase in the area per lipid and a reduction in the thickness of the bilayer (Fig. S11) when compared to when only the protein was present (Fig. S7). Moreover, hydroxyebastine does not have effects on the curvature induced by ASM itself on the bilayer (Fig. S11).

We observed that both hydroxyebastine and loratadine establish contact with the protein, with the latter especially showing an average of more than 20 % of loratadine atoms in contact with the protein after 500 ns of simulation time (Fig. 9C). Our analysis showed that the presence of hydroxyebastine or loratadine does not affect the conformation of the catalytic domain which largely retained the starting X-ray crystallography structure (Fig. S1). We then evaluated the binding modes of hydroxyebastine or loratadine on the ASM structure using a contact-based analysis previously described for ebastine, estimating the occurrence and persistency of the interaction of the different CAD

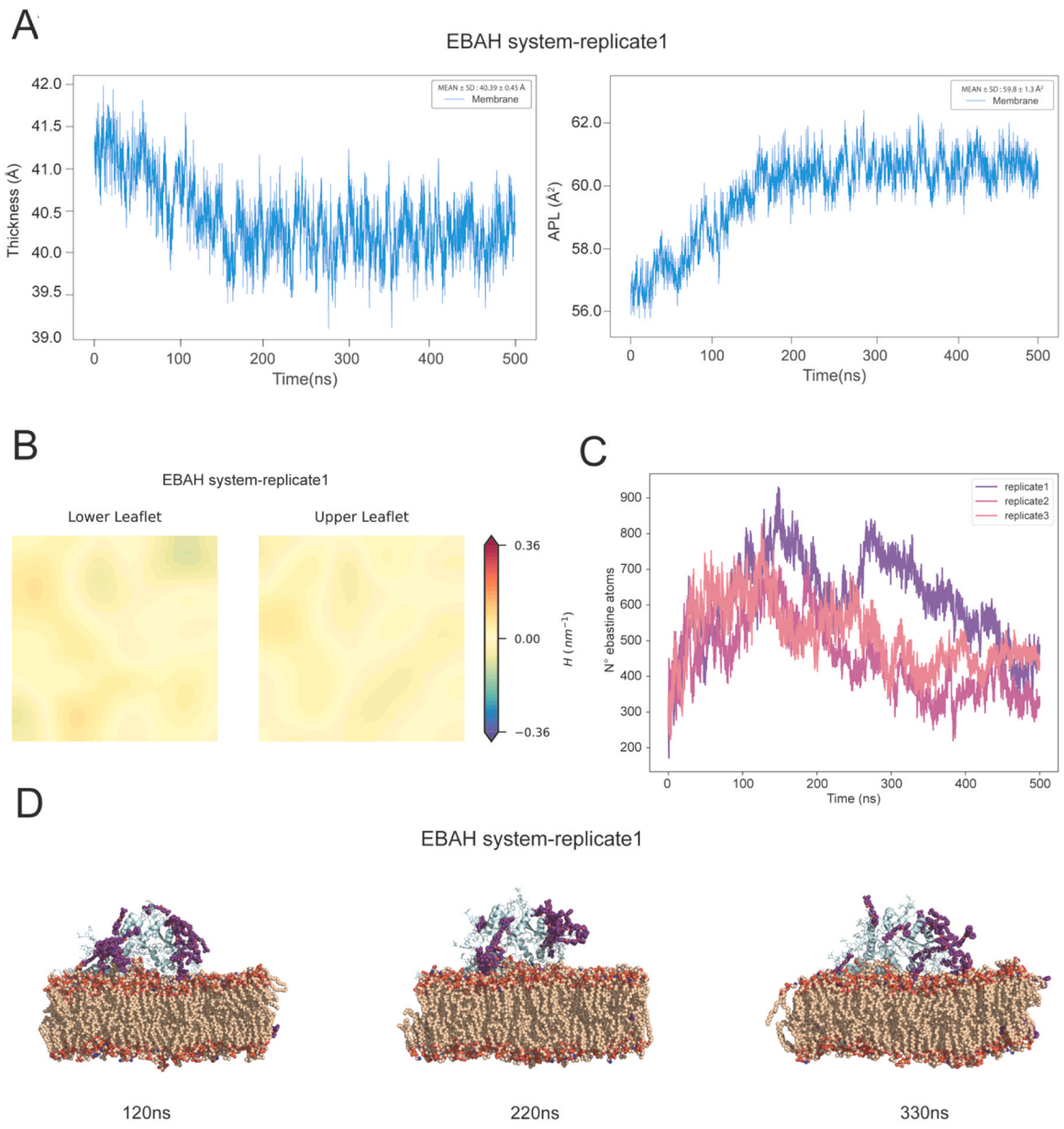

Fig. 7. Membrane biophysical properties in the presence of ebastine. (A) Average area per lipid (left panel) and lipid bilayer thickness (right panel) of replicate 1 of the EBAH system. Ebastine did not induce substantial changes in the thickness profiles of the EBAH, EBAH-ASM, and ASM model 1 simulations (Fig. S6-S7). Moreover, it induced only minor changes in both area per lipid and bilayer thickness compared to MD simulations in the absence of ebastine [32]. (B) Average mean curvature of the lower (left panel) and upper (right panel) leaflets of the bilayer calculated for replicate 1 of the EBAH system. Negative and positive mean curvature are indicated in blue and red, respectively. Ebastine did not induce any specific strong positive or negative curvature in the bilayer. (C) Number of ebastine atoms in contact with the protein or the N-glycans over time in the EBAH-ASM replicates. (D) Three representative structures were extracted at 120 ns, 220 ns, and 330 ns from replicate 1 of the EBAH-ASM simulation. ASM is depicted as a light blue cartoon, with lipids shown as spheres, and ebastine molecules as purple spheres. Ebastine formed high-occurrence contacts with ASM within the first 200 ns of simulation time, followed by a decrease as more ebastine molecules detached from the protein.

molecules with ASM and its pockets (Fig. 9D and S11). We observed that both hydroxyebastine and loratadine bind to several different regions of the protein with variable occurrence and several events of formation/breaking of the interactions. More than 50 % of loratadine molecules interact with ASM, limiting their membrane insertion when compared to ebastine and hydroxyebastine (Figs. 8A and 9D). In addition, we observed the tendency of forming interactions with some of the interfaces for membrane association while we identified no interaction in the proximity of the active site. Furthermore, hydroxyebastine and loratadine interact with the β1-α1 loop and reduce its lipid contacts (Fig. 9E), showing a similar tendency as ebastine (Fig. 8C).

Our results overall suggest that CADs can embed in the bilayer and interfere with its properties and with the association of ASM with the lysosomal membrane.

4. Conclusions

In this study, we investigated the interaction of ASM with lysosomal membranes using microsecond all-atom molecular dynamics. We also modeled the effects of ebastine, hydroxyebastine and loratadine as representatives of cationic amphiphilic drugs on the lysosomal membrane and ASM associated with the membrane. In our simulations, we accounted for the fully glycosylated form of ASM [33], and we designed a bilayer that mimics the lipid composition of typical lysosomal

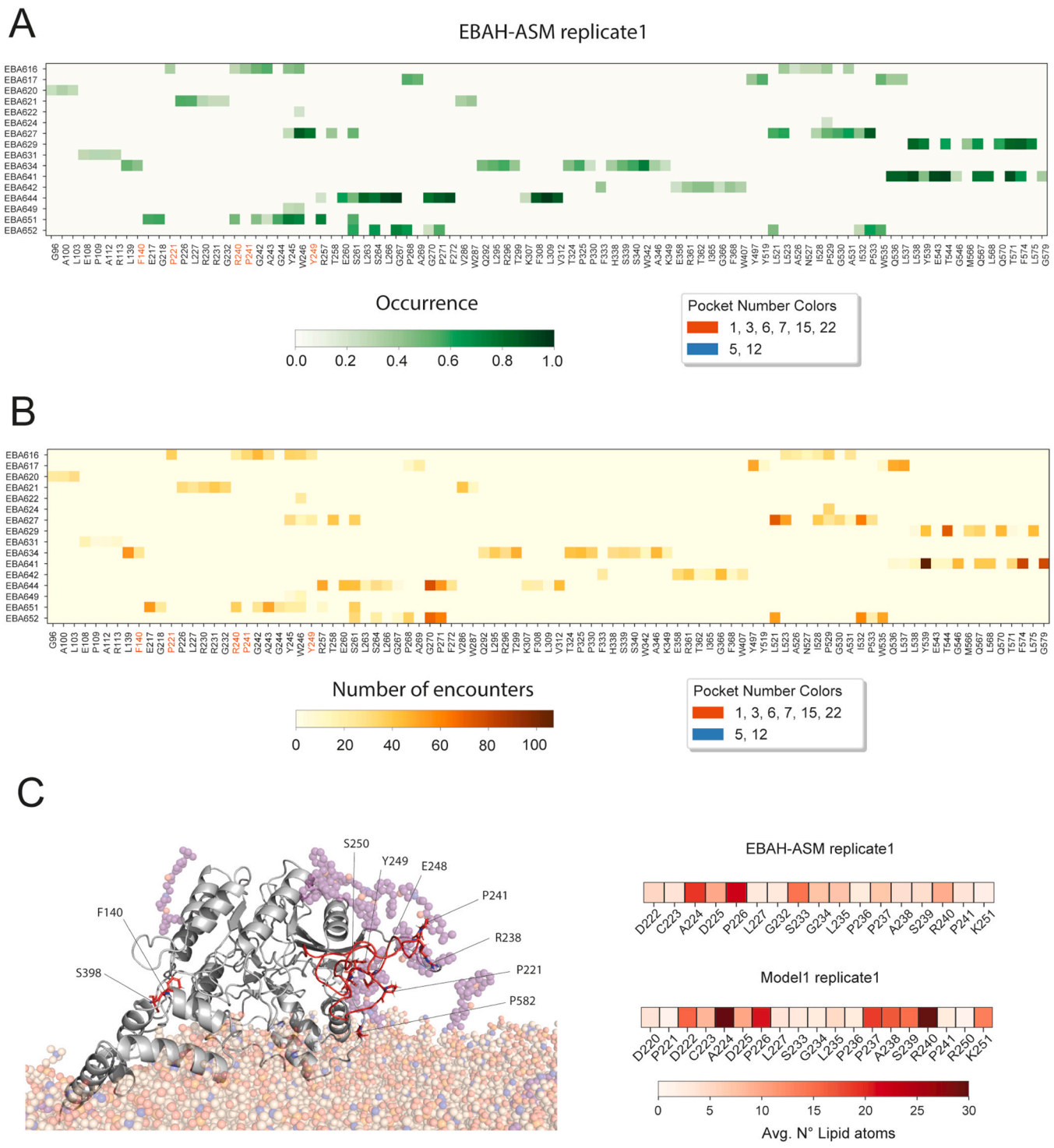

Fig. 8. Ebastine interacts with ASM and interferes with its membrane binding. (A-B) The heatmaps show the occurrence (A) and the number of encounters (B) of the contacts between ebastine molecules and the residues of ASM in replicate 1 of the EBAH-ASM system. The heatmaps report only ebastine-protein contacts occurring in at least 20 % of the simulation frames. Residues located in the pockets that correspond to membrane-binding regions or those near the catalytic site are highlighted in dark orange and blue, respectively. (C) The left panel displays a representative structure extracted at 500 ns from replicate 1 of the EBAH-ASM simulation. The protein is depicted as a gray cartoon with the β1-α1 loop in red, while the lipids are shown as light brown spheres and ebastine molecules are highlighted as purple spheres. Residues within the pockets that make contact with ebastine in any of the three replicates of EBAH-ASM are highlighted as red sticks. For clarity, *N*-glycans of the protein and all hydrogens are omitted. On the right panel, the heatmaps show the average number of lipid atoms in contact with the residues of the β1-α1 loop in replicate 1 of EBAH-ASM (upper heatmap) and model1 (lower heatmap). The observed reduction in the average number of lipids in contact with the protein suggests that ebastine molecules bind to ASM and interfere with the association to the membrane of the β1-α1 loop.

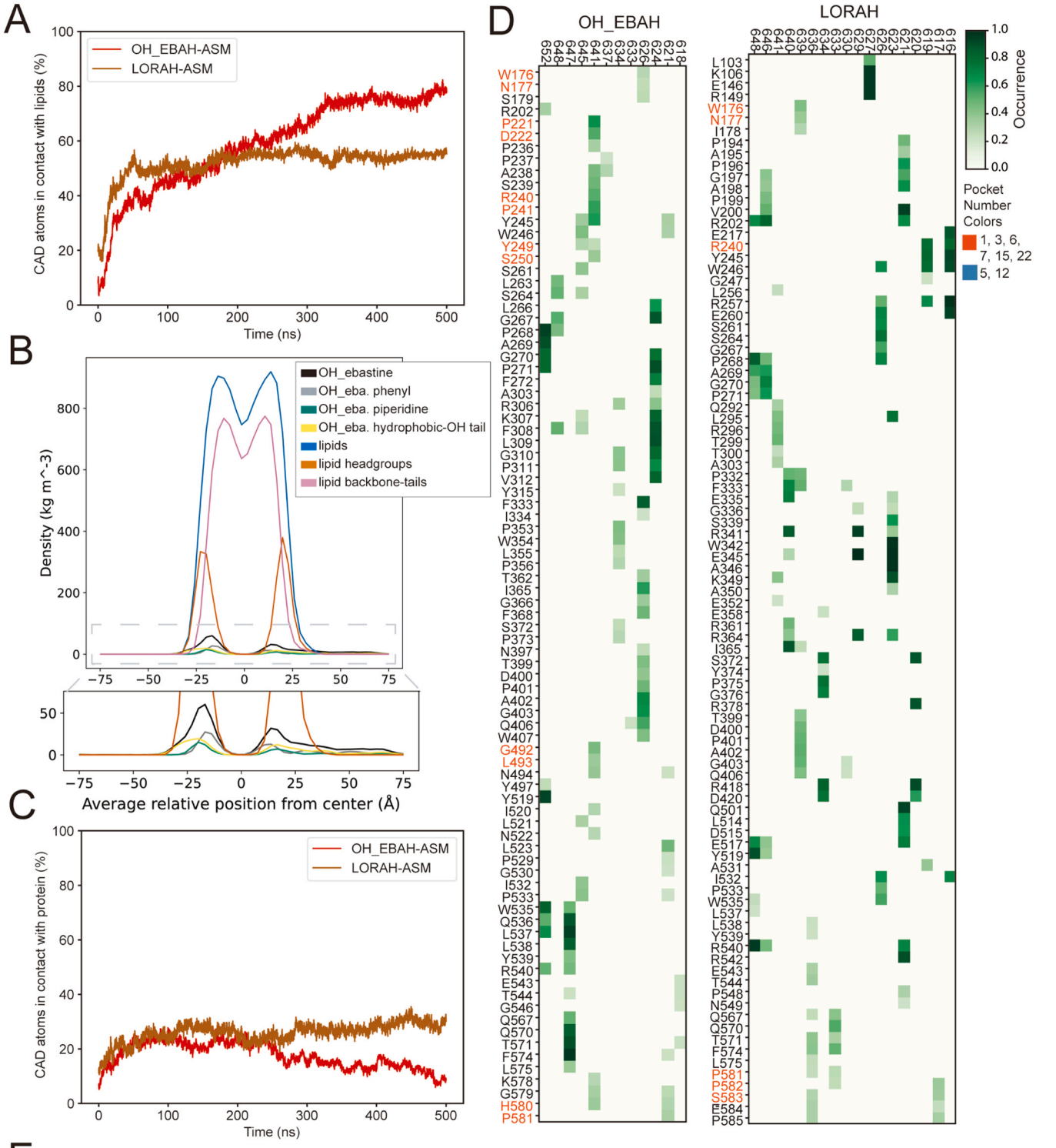

(caption on next page)

Fig. 9. Hydroxyebastine and loratadine interact with the lysosome-like bilayer and ASM and they interfere with membrane biophysical properties and binding. (A) Percentage of hydroxyebastine and loratadine atoms in contact with the lipid bilayer over time in the OH_EBAH-ASM and LORAH-ASM systems. We observed incomplete insertion of hydroxyebastine and loratadine molecules in the bilayer in the presence of ASM with ~70–80 % and ~55 % of hydroxyebastine and loratadine atoms, respectively, in contact with lipids after 400 ns of simulation time. (B) The mass density plots show how hydroxyebastine and the main components of lipids are distributed within the thickness of the lipid bilayer. The panels show the mass density profiles of i) all hydroxyebastine atoms (black), ii) hydroxyebastine phenyl groups (grey), iii) hydroxyebastine piperidine groups (green), iv) hydroxyebastine hydrophobic-OH tails (yellow), v) all lipid atoms (blue), vi) lipid headgroups (orange) and v) lipid backbone-tails (pink) along the axis perpendicular to the surface of the bilayer. The hydroxyebastine molecules insert at the interface between lipid headgroups and hydrophobic tails, with their phenyl groups preferentially orienting towards the lipid tails and the piperidine ring and the hydrophobic-OH tails more towards the lipid headgroups. (C) Percentage of hydroxyebastine and loratadine atoms in contact with the protein or the *N*-glycans over time in the OH_EBAH-ASM and LORAH-ASM systems. (D) The heatmaps show the occurrence of the contacts between hydroxyebastine (left panel) and loratadine (right panel) molecules and the residues of ASM in the OH_EBAH-ASM and LORAH-ASM systems. The heatmaps report only CADs-protein contacts occurring in at least 20 % of the simulation frames. Residues located in the pockets that correspond to membrane-binding regions or those near the catalytic site are highlighted in dark orange and blue, respectively. (E) The heatmaps show the average number of lipid atoms in contact with the residues of the β1-α1 loop in the OH_EBAH-ASM (left panel) and LORAH-ASM (right panel) systems. The observed reduction in the average number of lipids in contact with the protein when compared to ASM MD simulations (Fig. 8**C**) suggests that CAD molecules bind to ASM and interfere with the association to the membrane of the β1-α1 loop.

membranes from normal cells [57,58].

Overall, this work represented the first important step in developing a protocol to expand to other cationic amphiphilic drugs and membrane compositions. It also provided essential mechanistic insights into the structure of ASM associated with lysosomal membranes and the effects of CADs. In detail, our results confirm the type I association between the saposin domain of ASM and the lysosomal membrane observed with coarse-grained models [12]. Our data also support the role of N327, E390, and Y490 in the recruitment and orientation of the substrate lipids to the active site. In addition, the simulations also show that the ASM association with the lysosomal membrane changes the membrane curvature and promotes a dome-like shape beneath the active site, which could facilitate the recruitment of lipids to the active site.

Furthermore, the presence of different lipid species, including sphingomyelins, glycerophospholipids, ceramide-1-phosphate, and BMP in the catalytic site of the enzyme during the simulations supports the promiscuous phospholipase activity of ASM over a wide range of lipid species.

Ebastine generally interferes with the bilayer at the interface between lipid headgroups and their backbone-hydrophobic tails. In particular, ebastine hydrophobic tails are oriented towards the lipid tails of the lysosomal membrane, and the ebastine piperidine ring interacts with the lipid headgroups. This is consistent with what was observed for other lysosomotropic drugs [28] and amphiphilic drugs or natural compounds [63–66]. Furthermore, hydroxyebastine molecules interfere with the bilayer in a similar manner as ebastine but their hydrophobic-OH tails are preferentially oriented towards the lipid headgroups due to the presence of the polar hydroxy group that interacts with the lipid headgroups. On the other hand, loratadine shows a more incomplete insertion than ebastine and hydroxyebastine, being entrapped in interacting with ASM. In addition, we observed an enrichment of anionic lipids near the piperidine ring of ebastine, including phosphatidylinositol, phosphatidylserine species, and BMPs. Notably, it has been proposed that another CAD-like molecule, upon intercalation into membrane models, formed contact with phosphatidylserine species, mainly driven by electrostatic interactions with the lipid headgroups, and restricted their lateral diffusion, making them less available for the binding with peripheral membrane proteins [34,62].

According to the timescale and the membrane size and composition used in this study, we only observed minor changes in area per lipid and thickness induced by ebastine and hydroxyebastine and no changes in other membrane biophysical properties, which might require additional sampling or larger membrane constructs. Other factors could be related to the CADs/ratio used in this study. A future step should include additional simulations changing the ratio to observe dose-dependent effects, similar to what was done in other works [23,34].

Cation amphiphilic drugs are expected to cause alterations primarily to membranes of lysosomes from cancer cells, which often have alterations in lysosomal compositions with respect to lysosomes from normal cells, such as in their sphingolipid metabolism [6,30]. Thus, on one side, our results could also be interpreted as a genuine pattern of mild changes induced by ebastine and hydroxyebastine on normal lysosomal membranes. This is prompted by using a bilayer composition resembling one of the lysosomes in a non-transformed form. A future natural step would be to include data from lysosomal lipid profiling in cancer cells using lipidomics and exploit techniques for organelle-level lipidomics [57,58] from cancer cells before and after CAD treatment, such as lipidomics data from leukemia cell lines [30].

To the best of our knowledge, it is still unclear if CADs can directly bind to ASM and other lysosomal hydrolases [14]. Our results show that ebastine, hydroxyebastine and loratadine can directly interfere with ASM, altering loops of the catalytic domain that anchor to the membrane. This can be the first step to destabilize the ASM association with the lysosomal membrane. We did not expect to observe a detachment of ASM from the lipid bilayer in the microsecond timescale sampled by the unbiased MD simulations. A larger sampling of the conformational space and enhanced sampling approaches, along with higher CAD concentrations, are needed to probe if molecules such as ebastine and other CADs could induce ASM dissociation from the lysosomal membrane.

In addition, the simulations of ASM with CAD representatives presented in this study support a model of action in which CADs could compete with the lysosomal hydrolases, such as ASM, in the binding to anionic lipids and neutralize the negative charges on the surface of the intraluminal lysosomal vesicles [6,14].

More broadly, our work provides a computational approach that can be applied to other CADs using the parameterization protocol provided here and the strategies for designing the initial configuration for MD, together with the tools from the LipidDyn package [35].

CRediT authorship contribution statement

Marja Jäättelä: Funding acquisition, Resources, Writing – review & editing. **Kenji Maeda:** Data curation, Writing – review & editing. **Matteo Lambrughi:** Data curation, Formal analysis, Methodology, Supervision, Validation, Visualization, Writing – original draft, Writing – review & editing. **Simone Scrima:** Data curation, Formal analysis, Investigation, Methodology, Validation, Visualization, Writing – original draft, Writing – review & editing. **Lorenzo Favaro:** Formal analysis, Validation, Visualization, Writing – review & editing. **Elena Papaleo:** Conceptualization, Funding acquisition, Investigation, Project administration, Resources, Supervision, Writing – original draft, Writing – review & editing.

Declaration of Competing Interest

None.

Data Availability

All the topologies, input files, force-field parameters and MD trajectories related to this publication are accessible at the OSF repository: https://osf.io/w25ep/. The scripts, raw data, and outputs associated with the analysis are accessible at the OSF repository: https://osf.io/w25ep/.

Acknowledgments

Our research has been supported by Danmarks Grundforskningsfond (DNRF125) and Novo Nordisk Fonden Bioscience and Basic Biomedicine (NNF20OC0065262) to the E.P. group and Novo Nordisk Fonden (NNF19OC0054296) to the M.J. group. Part of the MD simulations have been performed thanks to the Danish HPC Infrastructure Computerome2 access. We would like to thank Mikkel Rohde for fruitful discussions and comments.

Appendix A. Supporting information

Supplementary data associated with this article can be found in the online version at doi:10.1016/j.csbj.2024.05.049.

References

[1] Braulke T, Carette JE, Palm W. Lysosomal enzyme trafficking: from molecular mechanisms to human diseases. Trends Cell Biol 2023;34:198–210. https://doi.org/10.1016/j.tcb.2023.06.005.
[2] Patra S, Patil S, Klionsky DJ, Bhutia SK. Lysosome signaling in cell survival and programmed cell death for cellular homeostasis. J Cell Physiol 2023;238:287–305. https://doi.org/10.1002/jcp.30928.
[3] Settembre C, Perera RM. Lysosomes as coordinators of cellular catabolism, metabolic signalling and organ physiology. Nat Rev Mol Cell Biol 2023;25:223–45. https://doi.org/10.1038/s41580-023-00676-x.
[4] Qin Y, Ashrafizadeh M, Mongiardini V, Grimaldi B, Crea F, Rietdorf K, et al. Autophagy and cancer drug resistance in dialogue: Pre-clinical and clinical evidence. Cancer Lett 2023;570:216307. https://doi.org/10.1016/j.canlet.2023.216307.
[5] Sandhoff R, Sandhoff K. Neuronal ganglioside and glycosphingolipid (GSL) metabolism and disease. Adv Neurobiol 2023;vol. 29:333–90. https://doi.org/10.1007/978-3-031-12390-0_12.
[6] Ellegaard A-M, Bach P, Jäättelä M. Targeting Cancer Lysosomes with Good Old Cationic Amphiphilic Drugs. Rev Physiol Biochem Pharmacol, vol. 185. Springer Science and Business Media Deutschland GmbH; 2020. p. 107–52. https://doi.org/10.1007/112_2020_56.
[7] Hämälistö S, Stahl JL, Favaro E, Yang Q, Liu B, Christoffersen L, et al. Spatially and temporally defined lysosomal leakage facilitates mitotic chromosome segregation. Nat Commun 2020;11:229. https://doi.org/10.1038/s41467-019-14009-0.
[8] Yang H, Tan JX. Lysosomal quality control: molecular mechanisms and therapeutic implications. Trends Cell Biol 2023;33:749–64. https://doi.org/10.1016/j.tcb.2023.01.001.
[9] Breiden B, Sandhoff K. Acid sphingomyelinase, a lysosomal and secretory phospholipase C, is key for cellular phospholipid catabolism. Int J Mol Sci 2021;22:9001. https://doi.org/10.3390/ijms22169001.
[10] Kornhuber J, Rhein C, Müller CP, Mühle C. Secretory sphingomyelinase in health and disease. Biol Chem 2015;396:707–36. https://doi.org/10.1515/hsz-2015-0109.
[11] Zhou Y-F, Metcalf MC, Garman SC, Edmunds T, Qiu H, Wei RR. Human acid sphingomyelinase structures provide insight to molecular basis of Niemann–Pick disease. Nat Commun 2016;7:13082. https://doi.org/10.1038/ncomms13082.
[12] Xiong Z-J, Huang J, Poda G, Pomès R, Privé GG. Structure of human acid sphingomyelinase reveals the role of the saposin domain in activating substrate hydrolysis. J Mol Biol 2016;428:3026–42. https://doi.org/10.1016/j.jmb.2016.06.012.
[13] Ferlinz K, Hurwitz R, Moczall H, Lansmann S, Schuchman EH, Sandhoff K. Functional characterization of the N-glycosylation sites of human acid sphingomyelinase by site-directed mutagenesis. Eur J Biochem 1997;243:511–7. https://doi.org/10.1111/j.1432-1033.1997.511_1a.x.
[14] Breiden B, Sandhoff K. Emerging mechanisms of drug-induced phospholipidosis. Biol Chem 2019;401:31–46. https://doi.org/10.1515/hsz-2019-0270.
[15] Hu M, Carraway KL. Repurposing cationic amphiphilic drugs and derivatives to engage lysosomal cell death in cancer treatment. Front Oncol 2020;10:605361. https://doi.org/10.3389/fonc.2020.605361.
[16] Iulianna T, Kuldeep N, Eric F. The Achilles' heel of cancer: targeting tumors via lysosome-induced immunogenic cell death. Cell Death Dis 2022;13:509. https://doi.org/10.1038/s41419-022-04912-8.
[17] Hämälistö S, Jäättelä M. Lysosomes in cancer—living on the edge (of the cell. Curr Opin Cell Biol 2016;39:69–76. https://doi.org/10.1016/j.ceb.2016.02.009.
[18] Zoncu R, Perera RM. Built to last: lysosome remodeling and repair in health and disease. Trends Cell Biol 2022;32:597–610. https://doi.org/10.1016/j.tcb.2021.12.009.
[19] Kornhuber J, Tripal P, Reichel M, Mühle C, Rhein C, Muehlbacher M, et al. Functional inhibitors of acid sphingomyelinase (FIASMAs): a novel pharmacological group of drugs with broad clinical applications. Cell Physiol Biochem 2010;26:9–20. https://doi.org/10.1159/000315101.
[20] Fogde DL, Xavier CPR, Balnytė K, Holland LKK, Stahl-Meyer K, Dinant C, et al. Ursolic acid impairs cellular lipid homeostasis and lysosomal membrane integrity in breast carcinoma cells. Cells 2022;11:4079. https://doi.org/10.3390/cells11244079.
[21] Petersen NHT, Olsen OD, Groth-Pedersen L, Ellegaard A-M, Bilgin M, Redmer S, et al. Transformation-associated changes in sphingolipid metabolism sensitize cells to lysosomal cell death induced by inhibitors of acid sphingomyelinase. Cancer Cell 2013;24:379–93. https://doi.org/10.1016/j.ccr.2013.08.003.
[22] Liu B, Chen R, Zhang Y, Huang J, Luo Y, Rosthøj S, et al. Cationic amphiphilic antihistamines inhibit STAT3 via Ca2+-dependent lysosomal H+ efflux. Cell Rep 2023;42:112137. https://doi.org/10.1016/j.celrep.2023.112137.
[23] Mehrabi SF, Elmi S, Nylandsted J. Repurposing phenothiazines for cancer therapy: compromising membrane integrity in cancer cells. Front Oncol 2023;13:1320621. https://doi.org/10.3389/fonc.2023.1320621.
[24] Ellegaard A-M, Dehlendorff C, Vind AC, Anand A, Cederkvist L, Petersen NHT, et al. Repurposing cationic amphiphilic antihistamines for cancer treatment. EBioMedicine 2016;9:130–9. https://doi.org/10.1016/j.ebiom.2016.06.013.
[25] Walker AJ, Card T, Bates TE, Muir K. Tricyclic antidepressants and the incidence of certain cancers: a study using the GPRD. Br J Cancer 2011;104:193–7. https://doi.org/10.1038/sj.bjc.6605996.
[26] Nadanaciva S, Lu S, Gebhard DF, Jessen BA, Pennie WD, Will Y. A high content screening assay for identifying lysosomotropic compounds. Toxicol Vitr 2011;25:715–23. https://doi.org/10.1016/j.tiv.2010.12.010.
[27] Kazmi F, Hensley T, Pope C, Funk RS, Loewen GJ, Buckley DB, et al. Lysosomal sequestration (Trapping) of lipophilic amine (Cationic Amphiphilic) drugs in immortalized human hepatocytes (Fa2N-4 Cells. Drug Metab Dispos 2013;41:897–905. https://doi.org/10.1124/dmd.112.050054.
[28] Stark M, Silva TFD, Levin G, Machuqueiro M, Assaraf YG. The lysosomotropic activity of hydrophobic weak base drugs is mediated via their intercalation into the lysosomal membrane. Cells 2020;9:1082. https://doi.org/10.3390/cells9051082.
[29] Alakoskela J, Vitovič P, Kinnunen PKJ. Screening for the drug–phospholipid interaction: correlation to phospholipidosis. ChemMedChem 2009;4:1224–51. https://doi.org/10.1002/cmdc.200900052.
[30] Nielsen IØ, Groth-Pedersen L, Dicroce-Giacobini J, Jonassen ASH, Mortensen M, Bilgin M, et al. Cationic amphiphilic drugs induce elevation in lysoglycerophospholipid levels and cell death in leukemia cells. Metabolomics 2020;16:91. https://doi.org/10.1007/s11306-020-01710-1.
[31] Jo S, Kim T, Im W. Automated builder and database of protein/membrane complexes for molecular dynamics simulations. PLoS One 2007;2:e880. https://doi.org/10.1371/journal.pone.0000880.
[32] Pogozheva ID, Armstrong GA, Kong L, Hartnagel TJ, Carpino CA, Gee SE, et al. Comparative molecular dynamics simulation studies of realistic eukaryotic, prokaryotic, and archaeal membranes. J Chem Inf Model 2022;62:1036–51. https://doi.org/10.1021/acs.jcim.1c01514.
[33] Scrima S., Lambrughi M., Tiberti M., Fadda E., Papaleo E. ASM Variants in the Spotlight: A Structure-Based Atlas for Unraveling Pathogenic Mechanisms in Lysosomal Acid Sphingomyelinase n.d. ⟨https://doi.org/10.1101/2023.11.24.568551⟩.
[34] Heitmann ASB, Zanjani AAH, Klenow MB, Mularski A, Sønder SL, Lund FW, et al. Phenothiazines alter plasma membrane properties and sensitize cancer cells to injury by inhibiting annexin-mediated repair. J Biol Chem 2021;297:101012. https://doi.org/10.1016/j.jbc.2021.101012.
[35] Scrima S, Tiberti M, Campo A, Corcelle-Termeau E, Judith D, Foged MM, et al. Unraveling membrane properties at the organelle-level with LipidDyn. Comput Struct Biotechnol J 2022;20:3604–14. https://doi.org/10.1016/j.csbj.2022.06.054.
[36] Huang J, MacKerell AD. CHARMM36 all-atom additive protein force field: Validation based on comparison to NMR data. J Comput Chem 2013;34:2135–45. https://doi.org/10.1002/jcc.23354.
[37] Daura X, Gademann K, Jaun B, Seebach D, van Gunsteren WF, Mark AE. Peptide folding: when simulation meets experiment. Angew Chem Int Ed 1999;38:236–40. https://doi.org/10.1002/(SICI)1521-3773(19990115)38:1/2<236::AID-ANIE236>3.0.CO;2-M.
[38] Berendsen HJC, Postma JPM, van Gunsteren WF, DiNola A, Haak JR. Molecular dynamics with coupling to an external bath. J Chem Phys 1984;81:3684–90. https://doi.org/10.1063/1.448118.
[39] Evans DJ, Holian BL. The nose–hoover thermostat. J Chem Phys 1985;83:4069–74. https://doi.org/10.1063/1.449071.
[40] Parrinello M, Rahman A. Polymorphic transitions in single crystals: a new molecular dynamics method. J Appl Phys 1981;52:7182–90. https://doi.org/10.1063/1.328693.
[41] Nosé S, Klein ML. Constant pressure molecular dynamics for molecular systems. Mol Phys 1983;50:1055–76. https://doi.org/10.1080/00268978300102851.
[42] Hess B, Bekker H, Berendsen HJC, Fraaije JGEM. LINCS: a linear constraint solver for molecular simulations. J Comput Chem 1997;18:1463–72. https://doi.org/10.1002/(SICI)1096-987X(199709)18:12<1463::AID-JCC4>3.0.CO;2-H.
[43] Darden T, York D, Pedersen L. Particle mesh Ewald: an $N \cdot \log(N)$ method for Ewald sums in large systems. J Chem Phys 1993;98:10089–92. https://doi.org/10.1063/1.464397.

[44] Essmann U, Perera L, Berkowitz ML, Darden T, Lee H, Pedersen LG. A smooth particle mesh Ewald method. J Chem Phys 1995;103:8577–93. https://doi.org/10.1063/1.470117.
[45] Kim S, Chen J, Cheng T, Gindulyte A, He J, He S, et al. PubChem in 2021: new data content and improved web interfaces. Nucleic Acids Res 2021;49:D1388–95. https://doi.org/10.1093/nar/gkaa971.
[46] Ropp PJ, Spiegel JO, Walker JL, Green H, Morales GA, Milliken KA, et al. Gypsum-DL: an open-source program for preparing small-molecule libraries for structure-based virtual screening. J Chemin- 2019;11:34. https://doi.org/10.1186/s13321-019-0358-3.
[47] Kallunki T, Olsen OD, Jäättelä M. Cancer-associated lysosomal changes: friends or foes. Oncogene 2013;32:1995–2004. https://doi.org/10.1038/onc.2012.292.
[48] Goldman SD, Funk RS, Rajewski RA, Krise JP. Mechanisms of amine accumulation in, and egress from, lysosomes. Bioanalysis 2009;1:1445–59. https://doi.org/10.4155/bio.09.128.
[49] O'Boyle NM, Banck M, James CA, Morley C, Vandermeersch T, Hutchison GR. Open babel: an open chemical toolbox. J Chemin- 2011;3:33. https://doi.org/10.1186/1758-2946-3-33.
[50] Vanommeslaeghe K, Hatcher E, Acharya C, Kundu S, Zhong S, Shim J, et al. CHARMM general force field: a force field for drug-like molecules compatible with the CHARMM all-atom additive biological force fields. J Comput Chem 2010;31:671–90. https://doi.org/10.1002/jcc.21367.
[51] Croitoru A, Park S-J, Kumar A, Lee J, Im W, MacKerell AD, et al. Additive CHARMM36 force field for nonstandard amino acids. J Chem Theory Comput 2021;17:3554–70. https://doi.org/10.1021/acs.jctc.1c00254.
[52] Michaud-Agrawal N, Denning EJ, Woolf TB, Beckstein O. MDAnalysis: a toolkit for the analysis of molecular dynamics simulations. J Comput Chem 2011;32:2319–27. https://doi.org/10.1002/jcc.21787.
[53] Abraham MJ, Murtola T, Schulz R, Páll S, Smith JC, Hess B, et al. GROMACS: high performance molecular simulations through multi-level parallelism from laptops to supercomputers. SoftwareX 2015;2:19–25. https://doi.org/10.1016/j.softx.2015.06.001.
[54] Fas BA, Maiani E, Sora V, Kumar M, Mashkoor M, Lambrughi M, et al. The conformational and mutational landscape of the ubiquitin-like marker for autophagosome formation in cancer. Autophagy 2021;17:2818–41. https://doi.org/10.1080/15548627.2020.1847443.
[55] Wilson KA, Wang L, Lin YC, O'Mara ML. Investigating the lipid fingerprint of SLC6 neurotransmitter transporters: a comparison of dDAT, hDAT, hSERT, and GlyT2. BBA Adv 2021;1:100010. https://doi.org/10.1016/j.bbadva.2021.100010.
[56] Mercadante D, Gräter F, Daday C. CONAN: a tool to decode dynamical information from molecular interaction maps. Biophys J 2018;114:1267–73. https://doi.org/10.1016/j.bpj.2018.01.033.
[57] Stahl-Meyer J, Holland LKK, Liu B, Maeda K, Jäättelä M. Lysosomal changes in mitosis. Cells 2022;11:875. https://doi.org/10.3390/cells11050875.
[58] Radulovic M, Wenzel EM, Gilani S, Holland LK, Lystad AH, Phuyal S, et al. Cholesterol transfer via endoplasmic reticulum contacts mediates lysosome damage repair. EMBO J 2022;41:e112677. https://doi.org/10.15252/embj.2022112677.
[59] Bilgin M, Nylandsted J, Jäättelä M, Maeda K. Quantitative profiling of lysosomal lipidome by shotgun lipidomics. Methods Mol Biol 2017;vol. 1594:19–34. https://doi.org/10.1007/978-1-4939-6934-0_2.
[60] Stahl-Meyer K, Bilgin M, Holland LKK, Stahl-Meyer J, Kirkegaard T, Petersen NHT, et al. Galactosyl- and glucosylsphingosine induce lysosomal membrane permeabilization and cell death in cancer cells. PLoS One 2022;17:e0277058. https://doi.org/10.1371/journal.pone.0277058.
[61] Gruenberg J. Life in the lumen: the multivesicular endosome. Traffic 2020;21:76–93. https://doi.org/10.1111/tra.12715.
[62] Broniec A, Gjerde AU, Ølmheim AB, Holmsen H. Trifluoperazine causes a disturbance in glycerophospholipid monolayers containing phosphatidylserine (PS): effects of pH, acyl unsaturation, and proportion of PS. Langmuir 2007;23:694–9. https://doi.org/10.1021/la061628b.
[63] Paloncýová M, DeVane R, Murch B, Berka K, Otyepka M. Amphiphilic drug-like molecules accumulate in a membrane below the head group region. J Phys Chem B 2014;118:1030–9. https://doi.org/10.1021/jp4112052.
[64] Róg T, Girych M, Bunker A. Mechanistic understanding from molecular dynamics in pharmaceutical research 2: lipid membrane in drug design. Pharmaceuticals 2021;14:1062. https://doi.org/10.3390/ph14101062.
[65] Kopeć W, Telenius J, Khandelia H. Molecular dynamics simulations of the interactions of medicinal plant extracts and drugs with lipid bilayer membranes. FEBS J 2013;280:2785–805. https://doi.org/10.1111/febs.12286.
[66] Cramariuc O, Rog T, Vattulainen I. Drug-lipid membrane interaction mechanisms revealed through molecular simulations. Curr Phys Chem 2012;2:379–400. https://doi.org/10.2174/1877946811202040379.